J. Fluid Mech. (1984), *vol.* 141, *pp.* 197–231
Printed in Great Britain

Simple three-dimensional vortex motions in coflowing jets and wakes

By A. E. PERRY AND D. K. M. TAN
University of Melbourne, Department of Mechanical Engineering,
Parkville, Victoria 3052, Australia

(Received 13 April 1983 and in revised form 26 November 1983)

The vortex patterns which occur in coflowing jets and wakes at moderate Reynolds numbers (of order 500) are examined in detail. Flow visualization is used in conjunction with a flying hot-wire system which allows instantaneous velocity vector fields to be rapidly measured and related to the smoke patterns. The structures were made perfectly periodic in time by artificial stimulation. The experiments were therefore completely deterministic. This newly developed data-acquisition technique does not require the use of Taylor's hypothesis for inferring patterns from a fixed streamwise position. It therefore allows the vector fields of rapidly evolving patterns to be produced. It also allows the phenomenon of three-dimensional vortex pairing to be studied. The classification of patterns and conjectured topologies made by Perry & Lim (1978*a*, *b*) and the interpretations of Perry, Lim & Chong (1980) and Perry & Watmuff (1981) are examined. In the light of more-detailed measurements, it is found that some of these interpretations require modification.

Vortex 'skeleton' models of the patterns are constructed and it is found that the Biot–Savart law gives vector fields which are in reasonable agreement with the experiments. It is also found that the power-spectral density of a periodic array of eddies can be explained in terms of potential flow vortices.

1. Introduction

Turbulent flow appears to consist of a random and complex array of interacting vortex loops. In the early stages of transition from laminar to turbulent flow, orderly arrays of vortex loops are often observed. The authors suggest than an understanding of these three-dimensional eddying motions is basic to an understanding of the physics of transition and turbulence phenomena. Very little is known, however, of even the simplest orderly arrays of three-dimensional eddying motions. The aim of this work was to study such simple arrays in coflowing jets and wakes.

Studies of three-dimensional eddying motions have usually been hampered by randomness in the flow with a consequent loss of information in the averaging process. Perry & Lim (1978*a*, *b*) have, however, examined forced periodic coflowing jets and wakes at Reynolds numbers of the order 1000. By laterally perturbing a glass tube from which smoke was issuing, they were able to lock in the naturally occurring eddying motions to a fixed fundamental frequency in time. The eddying motions, made visible by the smoke, appeared frozen in time when viewed under stroboscopic light which was triggered in synchronism with the oscillation of the tube.

It will be seen that the near-perfect periodicity of these structures opens up many interesting ways of sampling the data from hot-wire probes placed in the flow.

It has been the aim of many workers (e.g. see Davies & Yule 1975; Falco 1977) to

measure entire instantaneous velocity vector fields surrounding eddying motions and to relate these fields with the smoke patterns. Perry, Lim & Chong (1980) were able to do this for two of the wake-type structures of Perry & Lim, using a sampling technique based on the phase of the tube oscillation. However, the technique they employed was fairly limiting in that it required the use of Taylor's hypothesis (measurements were taken at two fixed streamwise locations). It was therefore unsuitable for the jet-type structures, which grew and changed their shape rapidly with streamwise distance, or for flow situations where vortex pairing was occurring. They had also calibrated their hot wires statically, using the Roshko (1954) vortex-shedding method for low velocities. Calibrations were also assumed to be linear over the velocity range encountered. On the whole, their method was fairly time-consuming and experiments were often unsuccessful as the structures changed their shape with time and the hot-wire calibrations drifted in the time that was required to perform the experiment.

One aim of the present investigation was to develop an experimental technique to allow entire velocity vector fields about eddying motions to be measured in a streamwise plane of symmetry and to relate them to flow-visualization results. The technique had to achieve this with the minimum of assumptions and without the use of Taylor's hypothesis. It also had to perform the measurements within a six-minute period, since the structures remained stable for about six minutes before changes in the density of the smoke altered them. Also the wire calibrations altered noticeably after about 10 minutes of use in the smoke environment. Another aim was to study further the coherent structures of Perry & Lim.

2. Apparatus and procedure

2.1. *Apparatus*

Figure 1 shows the experimental arrangement used. Smoke issues from the glass tube which is aligned along the centreline of the wind tunnel. When the flow velocity U_e of the smoke exiting from the tube is slower than the velocity U_∞ of the surrounding fluid in the tunnel a coflowing wake is obtained. If the exit velocity exceeds the tunnel velocity a coflowing jet is obtained. In the case of wakes the eddies appear as loops which lean downstream, and in the case of jets these loops appear to lean upstream. These patterns, which occur naturally without any deliberate disturbance imposed on the flow, are best seen under stroboscopic light set approximately at the frequency of the patterns. The frequency and scale of the naturally occurring patterns modulate, and so even at Reynolds numbers as low as 500 there is considerable randomness in the flow. The jets and wakes produced can be single-sided or double-sided, i.e. the loops can appear on one or both sides of the jet or wake axis. It has been found by Anderson (1981) that, for sinusoidal oscillation of the tube in a plane, single-sided structures are produced by an asymmetric generation of vorticity at the source, e.g. by a misalignment of the tube outlet. Double-sided structures are produced by a symmetrical generation of vorticity.

Single-sided structures can also be produced by buoyancy effects, with the orientation of the structures being governed by the buoyancy force. When buoyancy effects are present, the tube can be oscillated vertically or horizontally without altering the structure orientation. However, the orientation of neutrally buoyant structures is determined by the direction of the forcing.

In the case of jets, U_∞ was typically 0.5 m/s and U_e was 1.3 m/s. In the case of wakes, U_e was 0^+ m/s and U_∞ was 0.5 m/s. If a sinusoidal signal is sent to the speaker

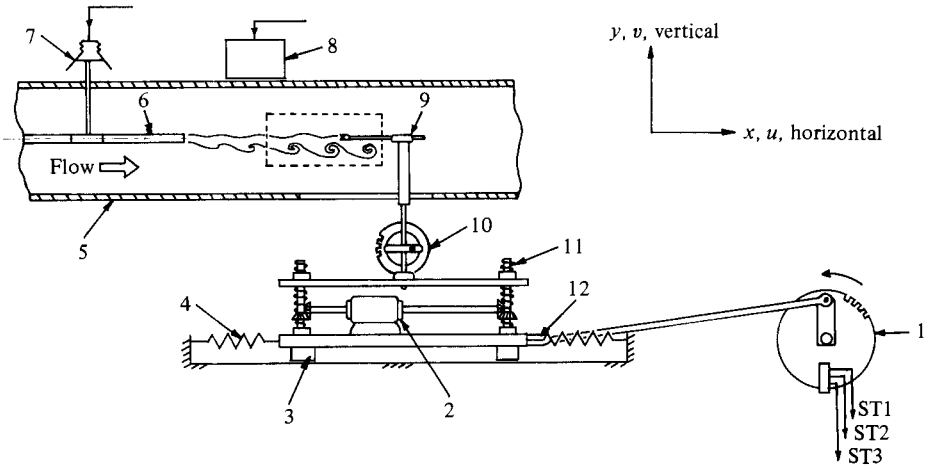

1. Slider–crank mechanism and 'chopper' disk
2. Stepping motor
3. Sled on air bearings
4. Retaining springs
5. Working section of tunnel
6. Glass tube
7. 'Woofer' speaker connected to glass tube
8. Stroboscope
9. Hot-wire probe
10. Scotch-yoke mechanism and 'chopper' disk (for vertical calibration)
11. Vertical feed screws
12. Vibration isolator coupling

FIGURE 1. Schematic diagram showing overall experimental setup and coordinate system used. Hot-wire sample grid boundary is shown as a dashed rectangle.

shown in figure 1, the maximum of the vertical perturbation velocity v' of the tube exit need only be $v'/U_\infty = 0.04$ for wakes or $v'/U_e = 0.05$ for jets, to produce near-perfect periodic flows which appear frozen under stroboscopic light triggered in synchronism with the tube oscillation. Furthermore, the shapes of the eddies are the same as those which occur naturally. The frequency used for wakes was typically 8 Hz and that for jets 28 Hz. Quite a range of frequencies ($\pm 50\%$ of these quoted values) could be used without significantly altering the shape of the eddies. Only their scale and spacing are altered. No discernible difference in the wake patterns were observed by varying the amplitude of oscillation provided that $v'/U_\infty < 0.2$. In the case of jets, the spreading rate appeared to increase monotonically with the amplitude of oscillation.

The smoke used for flow visualization was an oil vapour that was slightly heavier than the surrounding air. It was generated by a C. F. Taylor smoke generator. The generator had unsteady flow characteristics and it was isolated from the tunnel by filling a buffer tank with smoke, disconnecting the generator and then emptying the tank by displacing the smoke with a controlled flow of compressed air. Smoke was present throughout the measurements, which allowed photographs of the smoke patterns to be related directly to the measurements.

The tunnel was that used by Perry & Lim. The circular glass tube, which had an external diameter of 15 mm and an internal diameter of 13 mm, had its outlet modified by the addition of an aluminium sleeve which protruded 45 mm beyond the end of the glass tube. The sleeve had a sharp-edged elliptical outlet, aligned with the major axis horizontal and with a major to minor axis ratio of 20 mm/10 mm. Its use appeared to have no effect on the patterns except that of stabilizing the structure orientation and broadening the structures in the direction normal to the streamwise plane of symmetry (i.e. the z-direction, see figure 1 for coordinate system). Hot-wire

measurements, which were confined to this plane, were therefore less sensitive to any slight lateral wobbling of the structures. The sleeve was used for all flow cases studied. Perry & Lim had investigated the effect of the velocity profile inside the tube. Tubes between 10 and 130 diameters in length were tried without any significant changes in the structures.

Since Taylor's hypothesis was not be be used and time was a limiting factor in obtaining the measurements, a set of moving crossed wires were used. The wires measured the u- and v-components (as defined in figure 1) of velocity in the plane of symmetry. The hot-wire probe was mounted on a sting, which passed through a slot in the floor of the working section. The sting was mounted on a scotch-yoke mechanism, which was used only for calibration purposes. The scotch yoke was, in turn, mounted on a platform which rode on air bearings. The whole platform was oscillated back and forth by means of a slider–crank mechanism whose stroke could be varied from 25 to 110 mm. The large inertia forces that would be transmitted from the platform to the slider–crank were almost completely removed by horizontal restraining springs (as shown in figure 1). The whole system behaved as a spring–mass resonator. The platform could be traversed vertically (i.e. y-direction) by means of a stepping-motor screw-feed system which was under computer control.

Data were sampled on the upstream stroke of the wires. The frequency of oscillation of the sled was typically 0.85–0.95 Hz, which was sufficient to ensure that the probe did not start sampling before its own wake from the previous return stroke was washed clear of it downstream. The setup allowed the rapid sampling of the flow along the streamwise direction and also had the advantage of an imposed bias velocity. This velocity reduced the angle of the velocity vectors relative to the crossed wires over most of the flow field, which improved the accuracy of the calibration technique employed. The method used truncated Taylor-series expansions for the calibration equations (for details see Perry 1982).

The wires were dynamically calibrated *in situ* (far from the wake of the tube). Vertical calibrations were done with the scotch-yoke mechanism, which imposed a known sinusoidal perturbation on the wires, and horizontal calibrations were done with the slider–crank mechanism. The calibration technique was similar to that used by Perry & Watmuff (1981). Owing to the extremely low velocities encountered, the method of calibration was modified such that it did not require the use of a Pitot-static tube. This involved the so-called 'bootstrapping' method. The method relies on the fact that, when the velocity of the flow over a hot wire is close to zero, the sensitivity of that wire becomes very high. Zero velocities can therefore be easily detected to within ± 5 mm/s. The method is based on the principle of oscillating the wire along the working section of the tunnel at a known velocity (which will have a sinusoidal-like distribution since it is done by a slider–crank). The tunnel velocity is first set such that the minimum of the hot-wire voltage waveform corresponds to zero velocity. This occurs if the wires are momentarily moving downstream with the same velocity as the flow. This would occur at approximately the midpoint of the downstream stroke. Since the sled velocity is known accurately at all instances, the tunnel velocity is then known and other velocity–voltage pairs are generated through the rest of the probe oscillation cycle. The tunnel velocity is then increased to some new known value, within the range of the calibration just performed, and a new set of velocity–voltage pairs can be generated again. The process is repeated until the required range of velocities is covered. Third-order polynomial curve fits were used for the calibrations (i.e. for the velocity-versus-voltage curves), and the first- and higher-order terms were evaluated from the sensitivities determined from the dynamic calibration.

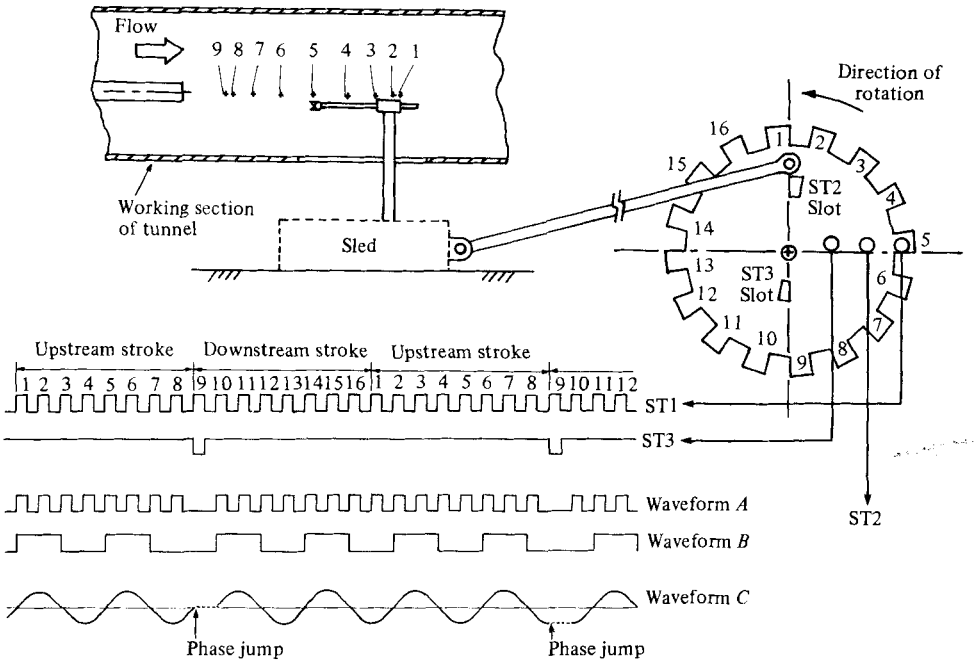

FIGURE 2. Schematic diagram illustrating data-acquisition method.

An analysis of the calibration technique and electronic circuitry used was conducted. It was found that velocity magnitudes could be measured to an accuracy of $\pm 3\%$ and the angle of velocity vectors could be measured to within $\pm 2°$. Further details on this and on the calibration method can be found in Tan (1983).

2.2. *Data acquisition*

Data were sampled at predetermined streamwise positions along the tunnel. This was done at one horizontal level (i.e. at a fixed y) for eight strokes of the slider–crank mechanism. The probe was then moved to the next level and the process repeated, and so on until the desired number of levels were sampled. It produced vector fields of a number of phases within a six-minute period, allowing animations of the vector fields to be constructed with computer graphics.

The principle behind the data-acquisition method is best explained with a simple example. Assume for simplicity that the chopper disk on the slider–crank has 16 equispaced slots on it, as shown in figure 2. Each slot produces a pulse which triggers the computer for sampling. These pulses will be referred to as ST1 pulses. Since sampling is carried out only on the upstream stroke, 8 consecutive pulses will be used for triggering the computer for sampling; these correspond with the first 8 streamwise positions shown in the figure. The chopper disk also produces other pulses – ST2 pulses, which are used to initialize the computer sampling at the commencement of each upstream stroke, and ST3 pulses, which are inverted and then summed with the ST1 pulses. This produces the waveform labelled A in figure 2. Waveform A is then frequency divided to produce waveform B, which is then low-pass filtered to produce the sinusoid labelled C. Note that the sinusoid has a phase jump of 90° every 3.75 cycles. This sinusoid is used to oscillate the glass tube. Figure 3 shows the circuit that is used to generate the various waveforms. If each cycle of oscillation is divided into 4 phases, the computer would sample phase 1 at position 1, phase 2 at position 2, etc. on the first stroke. On the next stroke, it would sample phase 4 at position

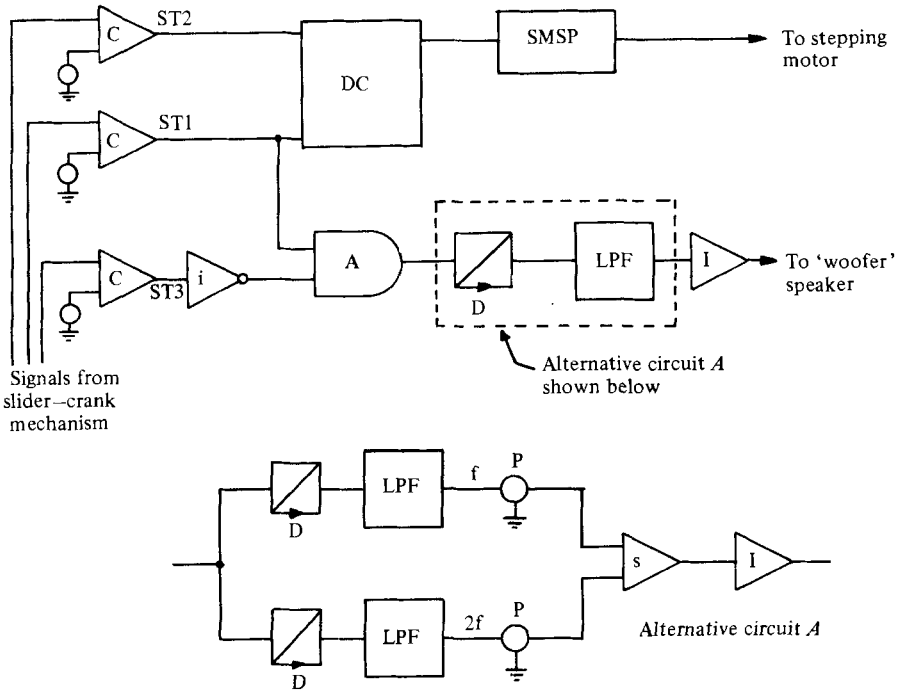

A – AND gate
C – comparator
D – frequency divider
I – current amplifier
i – inverter
s – analog summer
P – potentiometer
DC – digital computer
LPF – low-pass filter
SMSP – stepping-motor signal processor

FIGURE 3. Circuit diagram used for signal processing. Alternative circuit *A* used for vortex-pairing experiments.

1, phase 1 at position 2, etc.... The sampling sequence is shown in a 'timing diagram' in table 1 (*a*), where the numbers in the tabulation correspond to stroke numbers. After 4 strokes, data at all 4 phases would be otained at each position. The hot wires can then be moved to the next level and the process repeated.

The actual experiment followed the principle outlined above, but involved greater complexity. Phase jumping again occurred at the end of every upstream stroke, but there were 256 ST1 pulses and each cycle of the tube oscillation was divided into 32 phases. Two frequency dividers were used, giving tube oscillations of either $8f_s$ or $32f_s$, where f_s was the frequency of oscillation of the slider–crank. The phase jump was always 45° which, depending on the desired frequency of tube oscillation, required different widths of ST3 pulses. Tables 1 (*b*, *c*) show the timing diagrams for the $8f_s$ and $32f_s$ cases respectively. It can be seen that, for a given position, not all of the phases are sampled. An interpolation scheme was used to fill in the missing phases. Unlike the simple example outlined earlier, there were more cycles of tube oscillation between phase jumps. This allowed the transients associated with the phase jumping to fully decay before the start of a new sampling stroke.

2.3. *Smoothing*

It should be noted that only one data point is obtained for any given position and phase. In spite of the fact that the structures produced were very steady and

Phase / Position	1	2	3	4
1	1	4	3	2
2	2	1	4	3
3	3	2	1	4
4	4	3	2	1
5	1	4	3	2
6	2	1	4	3
7	3	2	1	4
8	4	3	2	1

(*a*)

Phase / Position	1	2	3	4	5	6	7	8	9	10	11	12	13	14	15	16	17	18	19	20	21	22	23	24	25	26	27	28	29	30	31	32
1	1				8				7				6				5				4				3				2			
2		1				8				7				6				5				4				3				2		
3			1				8				7				6				5				4				3				2	
4				1				8				7				6				5				4				3				2
5	2				1				8				7				6				5				4							
6		2				1				8				7																		
7			2				1				8				7																	
8				2				1				8																				
9	3				2				1																							
10		3				2																										
11			3				2																									
12				3																												
13	4				3																											
14		4																														
15			4																													
16				4																												
17	5																															

(*b*)

Phase / Position	1	2	3	4	5	6	7	8	9	10	11	12	13	14	15	16	17	18	19	20	21	22	23	24	25	26	27	28	29	30	31	32
1	1				8				7				6				5				4				3				2			
2	2				1				8				7				6				5				4				3			
3	3				2				1				8				7				6				5				4			
4	4				3				2				1				8				7				6							
5	5				4				3				2				1				8				7							
6	6				5				4				3				2				1											
7	7				6				5				4				3				2											
8	8				7				6				5				4															
9	1				8				7				6				5															
10	2				1				8				7																			
11	3				2				1																							
12	4																															
13	5																															
14																																

(*c*)

TABLE 1. (*a*) Timing diagram showing data sampled in example illustrating data-acquisition method. (*b*) Timing diagram for experiments where the tube is oscillated at $8f_s$. (*c*) Timing diagram for experiments where the tube is oscillated at $32f_s$. Numbers in diagram indicate the stroke number.

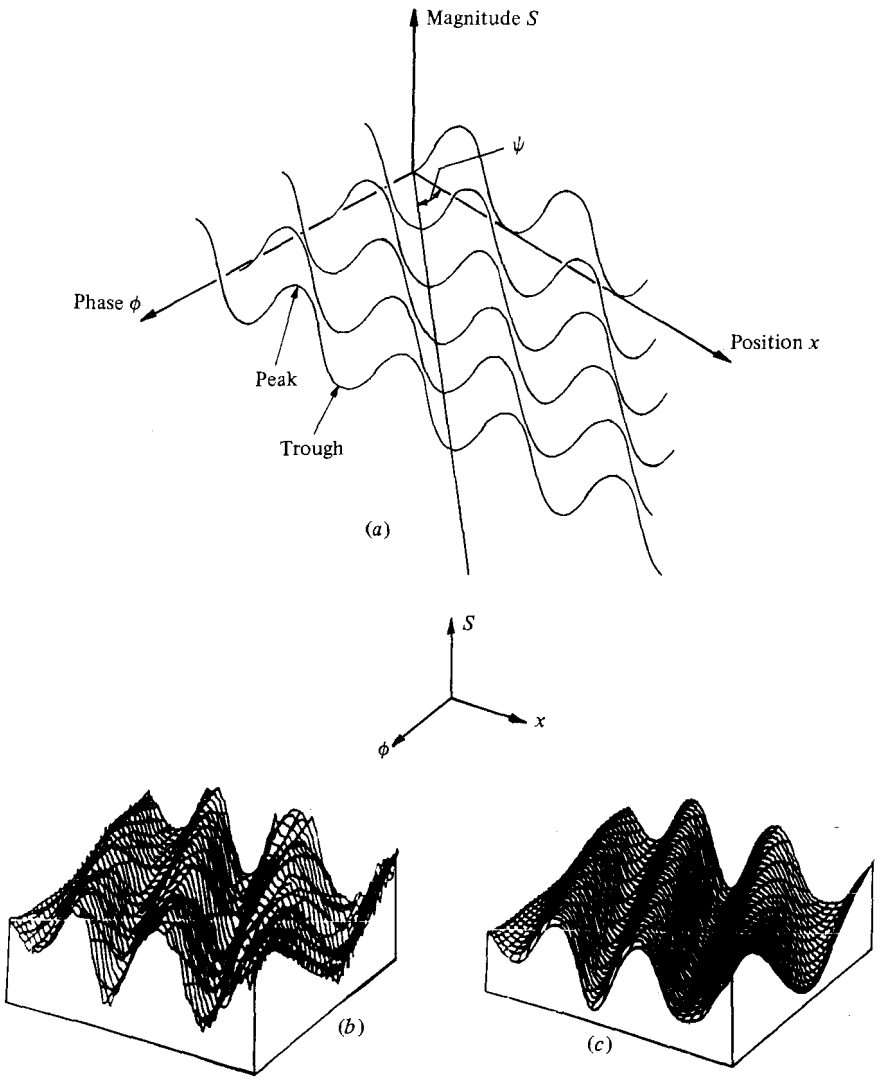

FIGURE 4. Three-dimensional phase/position/magnitude plots: (*a*) schematic; (*b*) experimental results (unsmoothed); (*c*) experimental (same results shown in (*b*), smoothed).

mechanical noise had been minimized, the data were smoothed. This was done primarily to allow the vorticity distribution to be computed without too much scatter. The smoothing procedure is described below and was designed to give a smooth transition from the vector field of one phase to the next phase. This had an additional advantage of producing a smoother animation.

After processing the data sampled and subtracting the bias velocity of the sled, a three-dimensional plot of velocity component S (i.e. either u or v) versus phase ϕ and position x can be produced for each level, as shown in figure 4. Fairly orderly rows of peaks and troughs at some angle ψ to the x-axis can be seen. This angle will give the 'convection' or 'phase' velocity of the structures. If the values of S were plotted along parallel lines at the angle ψ (see figure 4), straight lines parallel to the (ϕ, x)-plane should occur for the distributions of S if the structures were perfectly periodic in space and time. If the structures were growing and/or developing (i.e. they

were not perfectly periodic in space), the distribution would be some curve. Any noise on the signal would be observed as a higher-frequency fluctuation on the curve. The smoothing procedure is thus one of finding the convection velocity of the structures and performing a polynomial or Fourier-series curve fit to the distribution along lines at the angle ψ. By selecting the order of the curve-fit series, the higher-frequency components can be smoothed out.

The horizontal convection velocity of the structures was found as follows: The phase- or time-averaged values of S were subtracted and the perturbation s plotted as a function of ϕ and x. An even number n of x-positions were selected (usually 6 or 8, spread evenly over the range of x-positions sampled) and the correlation coefficient R, as defined below, was maximized by varying the parameter K:

$$R = \frac{\overline{s_1(\phi - Kx_1)\, s_2(\phi - Kx_2) \ldots s_n(\phi - Kx_n)}}{(\overline{s_1^n})^{1/n}\,(\overline{s_2^n})^{1/n} \ldots (\overline{s_n^n})^{1/n}}. \tag{1}$$

The overbars denote averaging over ϕ, and K is the gradient of the lines at angle ψ, i.e. $K = \mathrm{d}\phi/\mathrm{d}x$ (which has the dimensions of L^{-1}). The horizontal convection velocity U_ψ is given by

$$U_\psi = \frac{2\pi f}{K}, \tag{2}$$

where the frequency of oscillation f of the tube is in Hz, and the phase ϕ, in figure 4, is in radians.

If the structures under study were perfectly periodic in time and space, the resulting vector field relative to an observer moving with this convection velocity U_ψ will be steady. For the patterns here (which are growing and changing their shape), the vector fields measured relative to U_ψ are quasi-steady. However, this unsteadiness has been minimized.

The inferred convection velocity was found to vary slightly from one horizontal level to the next (typically by $\pm 5\,\%$). The average of all the convection velocities was used for the plots and this was found to correspond closely to the convection velocity of the foci in the flowfield. As mentioned earlier, the data points sampled were not evenly spaced in x but had a distribution corresponding to the probability density function for a slider–crank mechanism. Only about 40 % of the data sampled are presented in the vector fields. These points were chosen such that their distance apart was larger than a preselected value. This gave a more-even appearance to the data presented.

3. Experimental results and discussion

3.1. *Smoke patterns and vector fields*

Figure 5 (*a*) shows an externally illuminated photograph of a negatively buoyant wake (i.e. a single-sided wake with negative buoyancy). Figures 5 (*b–f*) show various views and laser-sectioned photographs which confirm the conjectures made by Perry & Lim (1978*a*, see their figure 9) concerning the smoke geometry. They had failed to obtain clear laser-sectioned photographs transverse to the wake axis.

The velocity vector field of this structure was obtained and is shown in figure 6 (*a*). The vector field has been plotted as seen by an observer with a negative vertical convection velocity V_ψ as well as the horizontal convection velocity U_ψ. The vertical convection velocity was estimated from the slope of the line passing through the centres of the vortices in the smoke photographs.

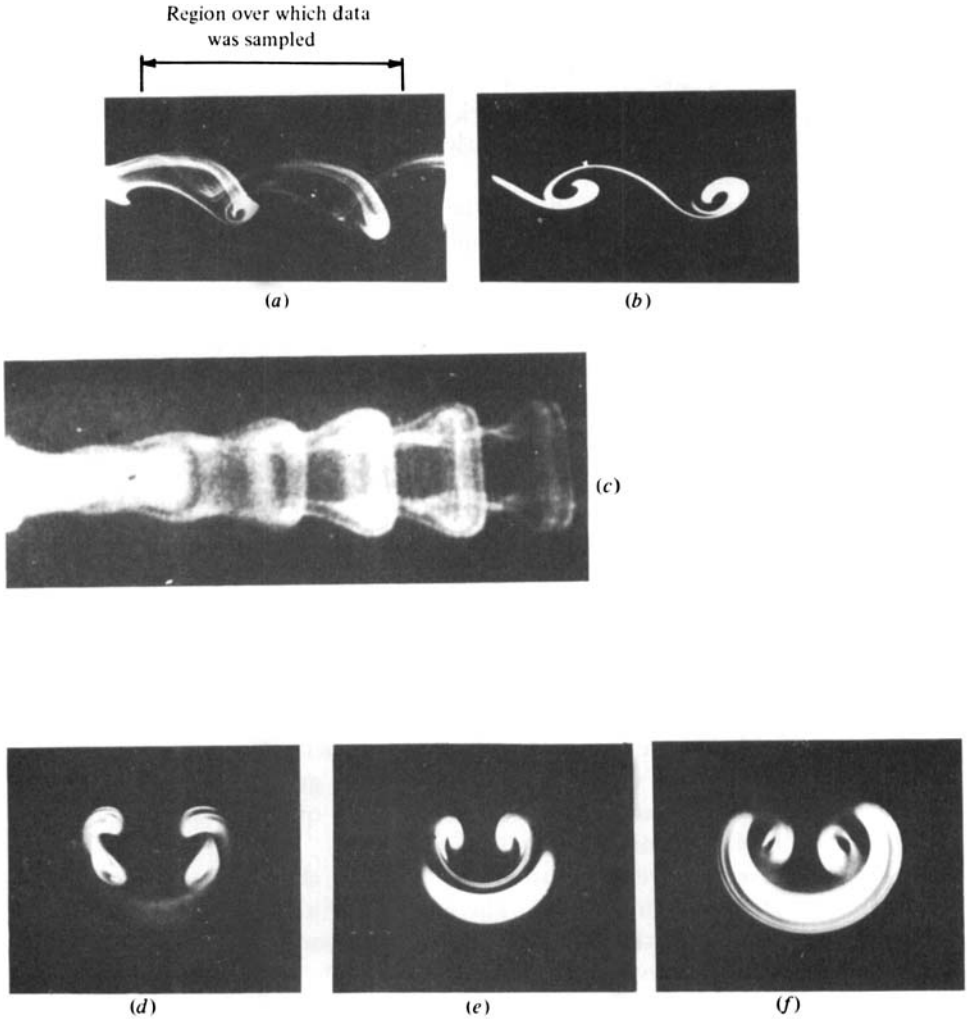

FIGURE 5. Negatively buoyant wake. (*a*) Externally illuminated photograph. (*b*) Laser-sectioned photograph. (*c*) Externally illuminated plan view (i.e. in $-y$-direction). (*d*), (*e*), (*f*) Transverse laser-sectioned photographs, i.e. progressive downstream sections of a structure (after Anderson 1981).

One useful tool in the description of vector fields is that of critical-point theory. A critical point in a flowfield is a point where the instantaneous streamline slope is indeterminate. These have been defined and classified in figure 2 of Perry *et al.* (1980), i.e. centres, foci, saddles, dislocated saddles (which sit on vortex sheets) and saddle–node combinations.

Figure 6(*b*) shows the same vector field as 6(*a*), but with only the direction of the vectors shown, i.e. the vector magnitude is fixed. Such a plot gives a clearer idea of the flow patterns in regions of very low velocity. The critical points, which are located in these regions, become much more obvious, e.g. the dislocated saddle labelled DS in the figure is very clear, as are the nodes and other saddles. The authors have found, however, that, in some cases, such a diagram can be misleading if it is used for inferring streamline patterns 'by eye'. In particular, it is very difficult to judge whether or not streamlines spiral into or out of foci. This property alone can affect the whole topology of the streamline pattern. It was therefore decided to develop a

method of computing instantaneous streamlines in order to remove some of the subjectivity. The results of this are shown in figure 6(*c*).

The instantaneous patterns were obtained by selecting the velocity vector field at the required instant (i.e. phase) and assuming that it was frozen in time. The equations

$$\frac{\mathrm{d}x}{\mathrm{d}t} = u = f_1(x, y), \quad \frac{\mathrm{d}y}{\mathrm{d}t} = v = f_2(x, y) \tag{3}$$

were then integrated numerically by a predictor–corrector method to give $x(t)$ and $y(t)$. Hence $y = f(x)$, which describes the instantaneous streamlines, was obtained. The functions $f_1(x, y)$ and $f_2(x, y)$ were obtained by fitting the data with 5th-order two-dimensional Taylor-series expansions. These were formed over rectangular regions, which will be referred to as 'tiles'. The size of the tiles were chosen such that they contained no more than two critical points (usually only one). The size of a typical tile is indicated in figure 6(*c*). If the tiles were too large, the method would sometimes generate extra critical points or it often removed existing ones. The boundaries between adjacent tiles overlapped. These regions of overlap ensured that the computed streamlines proceeded smoothly across the tile boundaries. A streamline which moves across to an adjacent tile was computed from the functions f_1 and f_2 of the first tile until it reached the midpoint of the region of overlap. Beyond this point, f_1 and f_2 of the second tile were used. One disadvantage of the Taylor-series fitting was that it smoothed the data, resulting in the smearing of vortex sheets and dislocated saddles. This can be seen by comparing figures 6(*b*) and (*c*). The dislocated saddle in figure 6(*b*) appears as a regular saddle in 6(*c*). Perhaps in further studies double Fourier series should be tried for the functions $f_1(x, y)$ and $f_2(x, y)$. Note that the vector fields can be regenerated from the fitted Taylor series. This was done for the figures 6(*c*), 7 and 11(*d*).

The streamline pattern is similar to that conjectured by Perry *et al.* except for the upper half of the flow. In the authors' results, the upper half of the flow contains a series of interconnected nodes and saddles. Each node and each saddle, which appears on the plane of symmetry, is part of a three-dimensional critical point which has been referred to as a saddle–node combination by Perry *et al.* and as a saddle–node trio by Hornung & Perry (1982) (see figures 2(*f*, *g*) in Perry *et al.*). The flow is probably irrotational in this region. If the origin of the coordinate system is positioned at each of these nodes and saddles in turn, a saddle occurring in the (x, y)-plane will appear as a node in the (x, z)-plane and *vice versa*. All such critical points appear as saddles in the (y, z)-plane. Thus sectional streamlines in the (y, z)-plane, i.e. the integral curves of the projections of vectors passing through the (y, z)-plane, will be as deduced by Perry *et al.* (shown in figure 6*d*). In the interpretation by Perry *et al.* the upper half of the flow contains a singular streamline. This streamline results from the intersection of two streamsurfaces. Details of such streamlines can be found in Hornung & Perry (1982).

It was found that the authors' results also yielded the pattern obtained by Perry *et al.* if the horizontal and vertical convection velocities were increased by about 10 %. This pattern is shown in figure 7, where the singular streamline is labelled *G*. Perry *et al.* had assumed the convection velocity U_ψ to be given by $U_\psi = f\lambda$, where f was the frequency of the stimulation signal and λ was the wavelength of the structures, as measured from the smoke photographs. The authors found that this method was somewhat subjective. In any case, if the patterns are non-periodic in space, there does not appear to be any single precisely defined convection velocity which is best for 'viewing' the patterns.

In the work of Perry *et al.*, the vortices were represented as foci 'in the large',

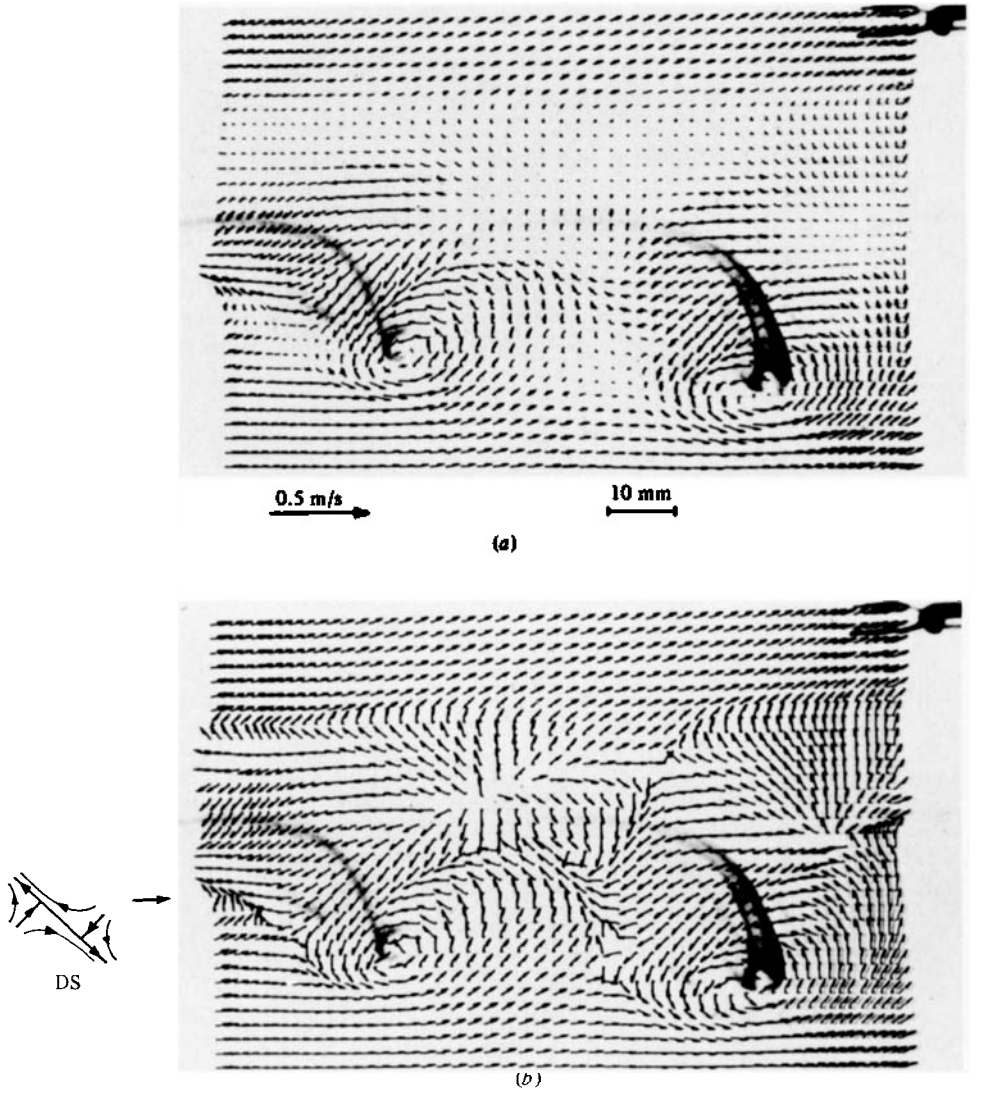

FIGURE 6(*a*, *b*). For caption see facing page.

asymptotically approaching centres as they spiral in. This was from the work of Perry & Fairlie (1974), who shows that steady inviscid critical points with finite vorticity were degenerate and locally two-dimensional – giving closed streamlines close to the 'eye' or the zero-velocity point of the vortex. However, it has been pointed out by Perry *et al.* that foci are possible in unsteady inviscid vortical flow where vortex stretching is occurring. The instantaneous streamlines spiral right into the eye of the vortex. Such patterns are also possible in a steady situation with constant-strain-rate stretching if viscosity is included in the analysis and if the stretching has persisted for a sufficient time (see Perry & Chong 1982; Batchelor 1967; Townsend 1951*a*,*b*; Hornung & Perry 1982). These foci patterns are locally three-dimensional and appear to be more appropriate than the rather hypothetical degenerate patterns. The velocity vectors also cross the smoke/air interface. This is

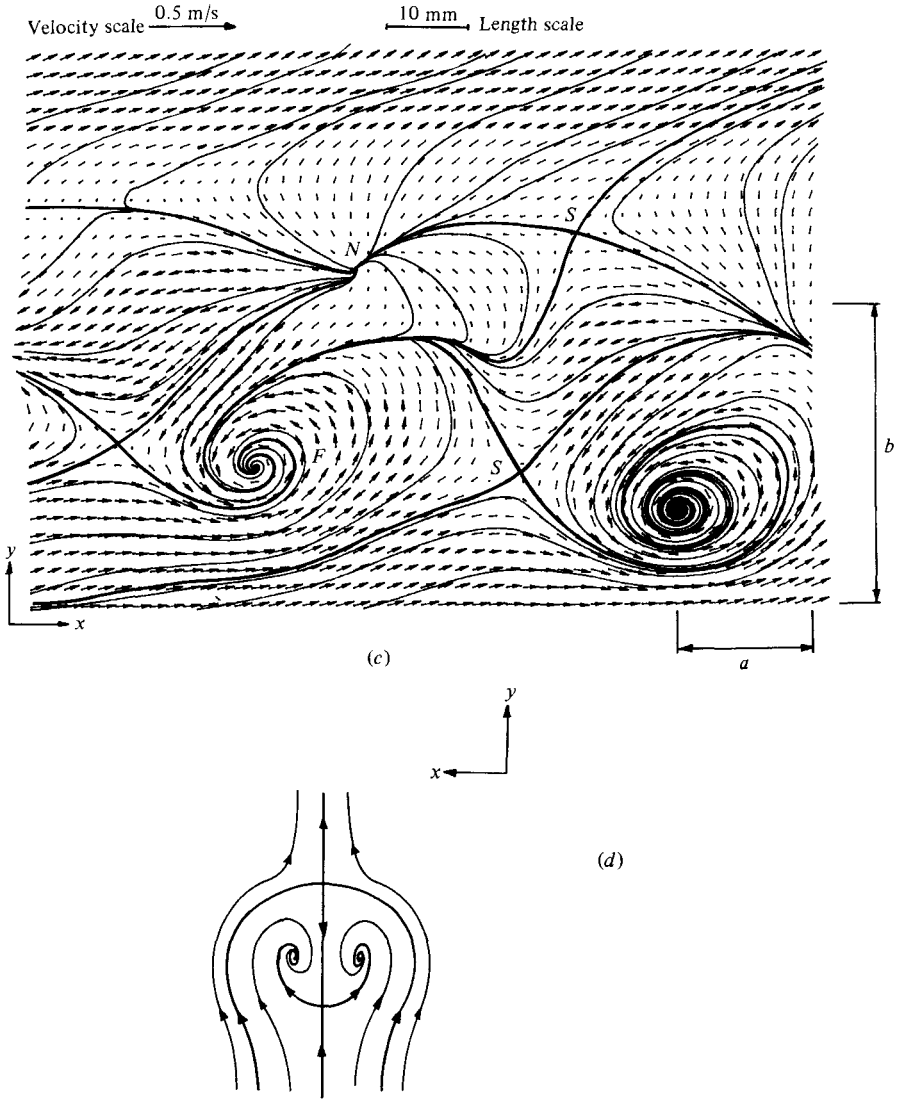

FIGURE 6. Negatively buoyant wake. (*a*) Vector field superimposed on smoke photograph. (*b*) Vector field (showing direction vectors only) superimposed on smoke photograph. Smoke photographs are shown in negative for clarity. (*c*) Streamline pattern computed from vector field shown in (*a*). Vector field shown is that obtained from the tiling procedure. (*d*) Conjectured sectional streamline pattern of Perry *et al.* $U_\infty \approx 0.47$ m/s, $U_\psi \approx 0.38$ m/s, $V_\psi \approx -0.025$ m/s, $f \approx 7.1$ Hz, Reynolds number (based on tube internal diameter and U_∞) ≈ 410. F, focus; N, node; S, saddle; DS, dislocated saddle; a and b in (*c*) are the dimensions of a typical tile.

possible since in unsteady flows, streaklines, hence vortex sheets, can move normal to themselves (Kline 1965).

The vector fields of two jet-type structures are shown in figures 8 and 9. Figure 8 shows a double-sided jet at the initial stages of instability ($v'/U_e \approx 0.05$). This is similar to the structures shown in figures 5 (*h*) and 11 (*b*) of Perry & Lim (1978*a*). Note that the freestream vectors below the smoke appear much smaller than those above the smoke. This is due to the structures being at the top end of the sample 'window'. The velocities at the top of the vector field had not reached freestream values, as can

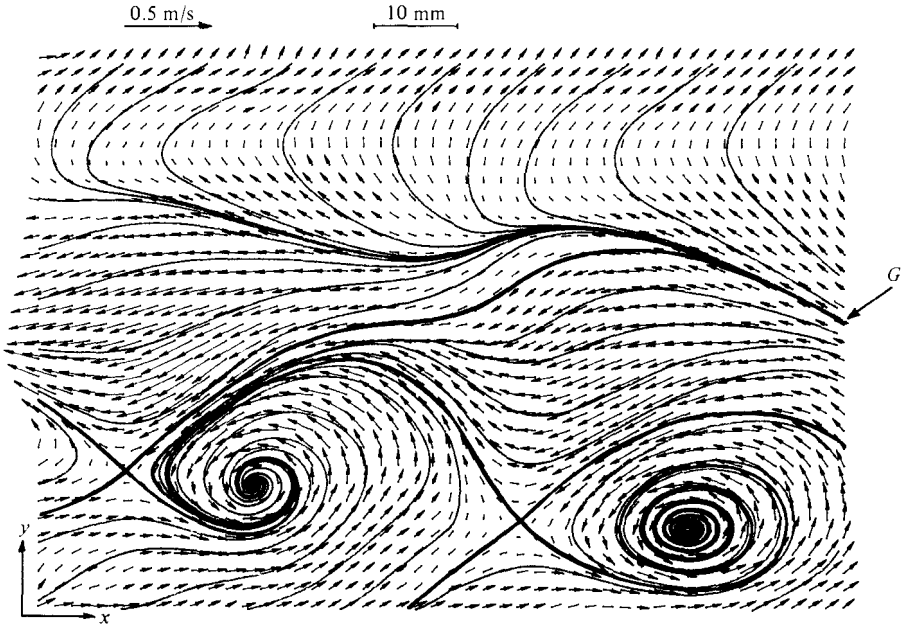

FIGURE 7. Streamline pattern computed from vector field shown in figure 6(*a*) with vertical and horizontal convection velocities 10% higher than that used for producing 6(*c*). Vector field shown is that obtained from the tiling procedure.

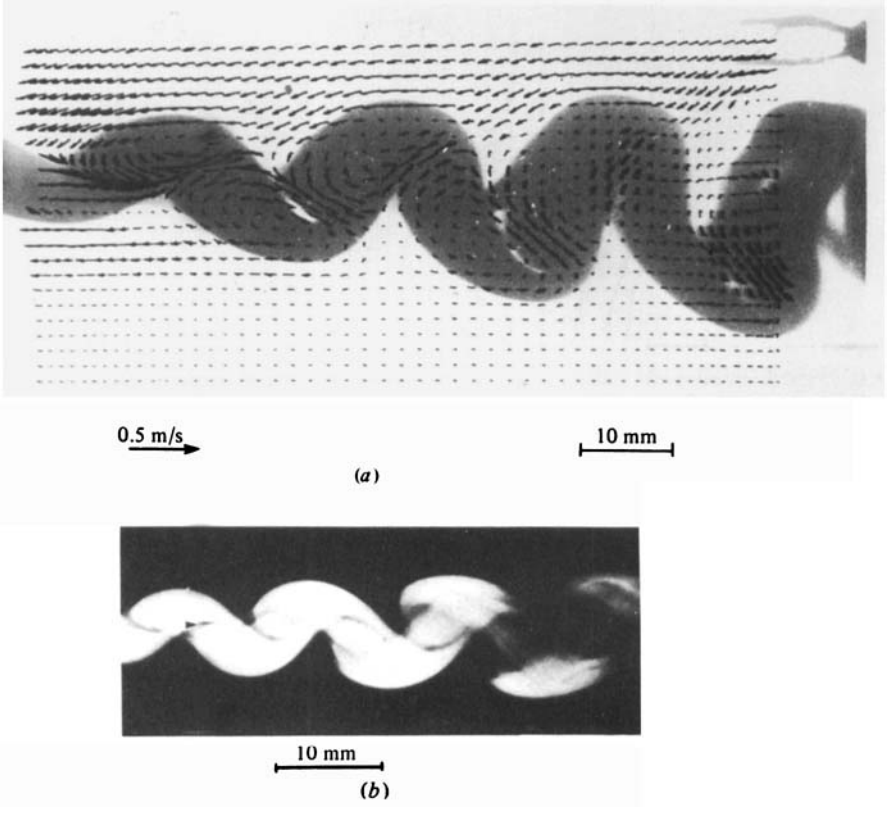

FIGURE 8(*a*, *b*). For caption see facing page.

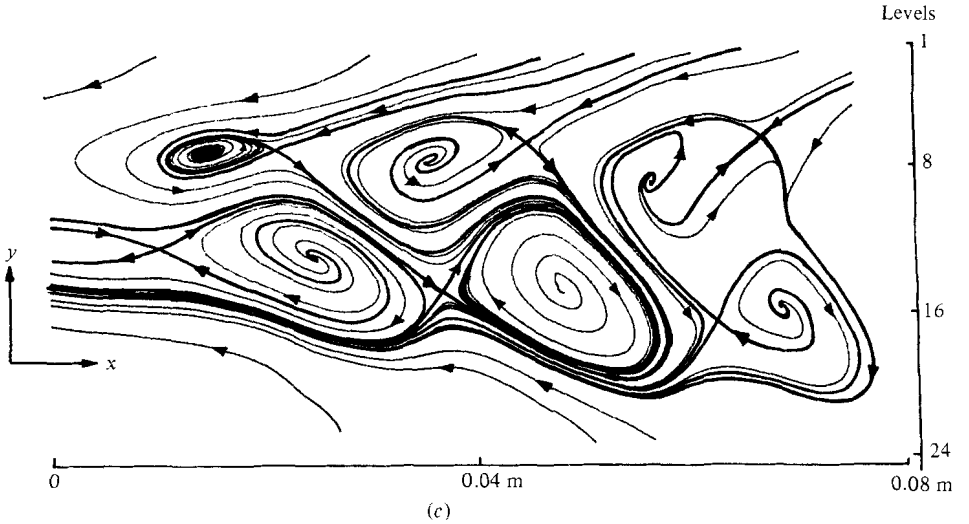

(*c*)

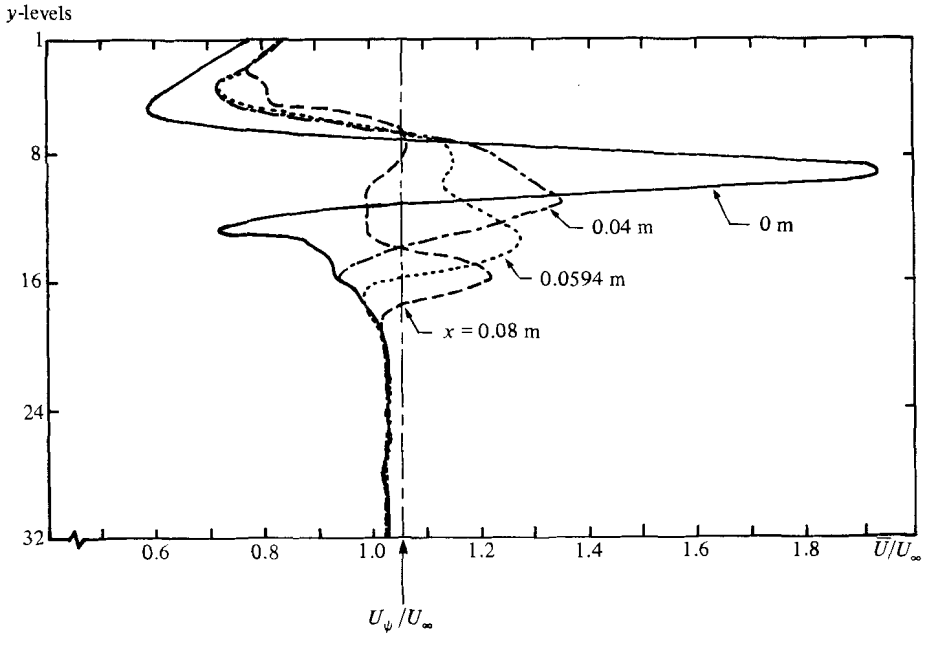

(*d*)

FIGURE 8. *Double-sided jet at initial stage of instability.* (*a*) Vector field superimposed on smoke photograph (smoke photograph is shown in negative for clarity). (*b*) Externally illuminated photograph of jet. (*c*) Streamline pattern computed from vector field shown in (*a*). (*d*) $\overline{U}$-distributions at various streamwise positions. $U_\infty \approx 0.62$ m/s, $U_\psi \approx 0.65$ m/s, $V_\psi \approx -0.04$, 0.02 m/s, $U_e \approx 1.2$ m/s, $f \approx 28.5$ Hz, Reynolds number (based on $U_e - U_\infty$) ≈ 510.

be seen from the time-averaged u profiles in figure 8(*d*) (i.e. $\overline{U} = \overline{u} + U_\psi$). There is also some asymmetry since the structure experiences buoyancy effects due to the smoke. Figure 9 shows another double-sided jet at a higher Reynolds number with $v'/U_\infty \approx 0.1$. It can be seen that the spreading rates are higher and the buoyancy effects are smaller. The growth rate of the jet is initially small but, at some fixed distance further downstream, the jet appears to split into two diverging rows of

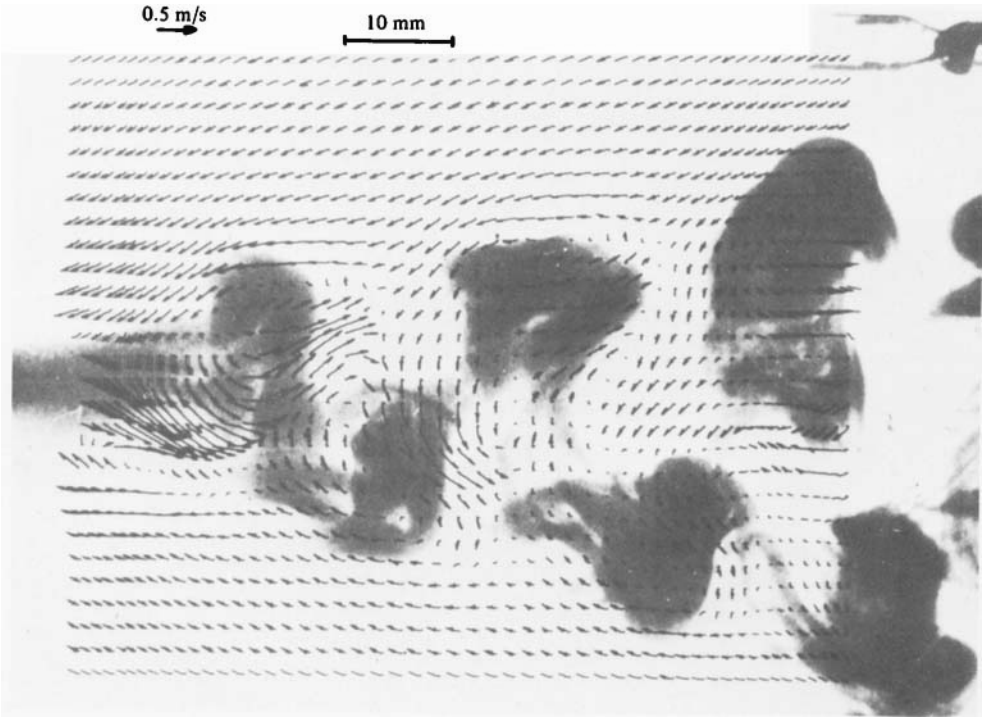

(a)

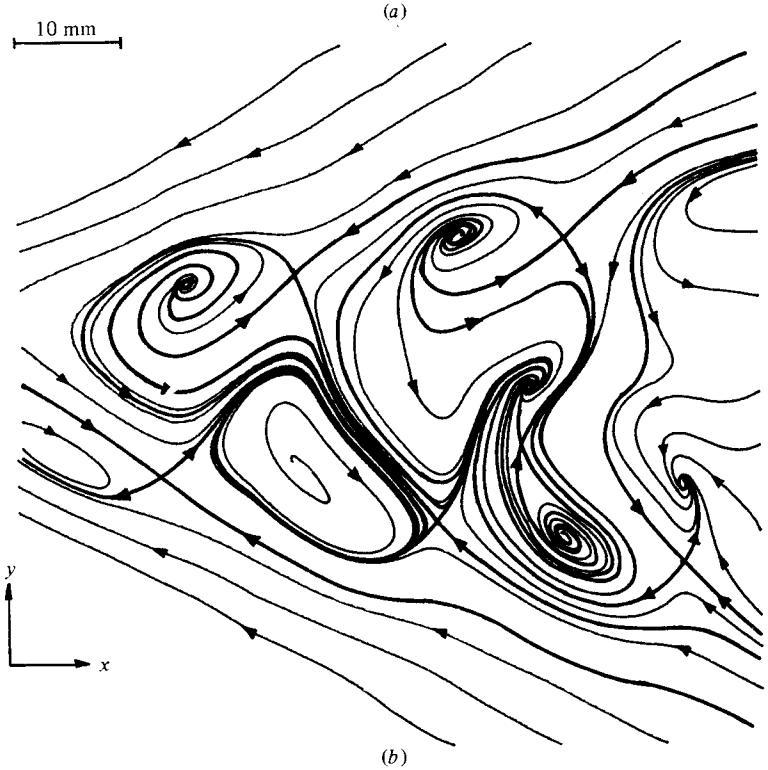

(b)

FIGURE 9. Double-sided jet (bifurcating). (a) Vector field superimposed on smoke photograph (smoke photograph is shown in negative for clarity). (b) Streamline pattern computed from vector field shown in (a). $U_\infty \approx 0.52$ m/s, $U_\psi \approx 0.68$ m/s, $V_\psi \approx -0.11$, 0.07 m/s, $U_e \approx 1.25$ m/s, $f \approx 27.9$ Hz, Reynolds number (based on $U_e - U_\infty$) ≈ 640.

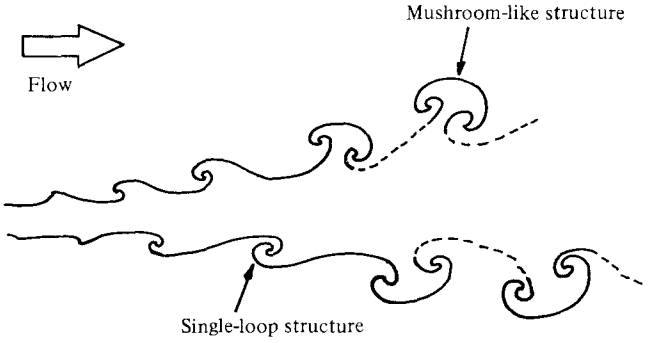

FIGURE 10. Sketch showing single-loop and mushroom-like structures. Note that the outlines joining the mushroom-like structures are shown as dashed lines since it is not clear from the smoke photographs how they are connected.

mushroom-like structures. This phenomenon, which can be seen very clearly in the ciné film of Perry & Lim (1978*b*), will be referred to as a bifurcation. This jet is similar to the structures shown in figures 7 (*a*, *b*) and 8 (*c*) in Perry & Lim (1978*a*). The features of the jet can be seen clearly, although the vectors do not line up as well with the smoke as in the case of the wake. This is mainly due to the difficulty encountered in the selection of an appropriate vertical convection velocity.

The horizontal spacing of the structures does not change much but vertical spacing does change, owing to spreading and/or bifurcation. The vector field of the wake was done with a vertical convection velocity. Selection of a vertical convection velocity for a jet is more difficult since different parts of it do not convect at the same rate. Since the jets are double-sided, the vector fields were done in two halves; the upper half with a positive vertical convection velocity and the lower half with a negative (estimated from the spreading angle of the structures as given by the smoke photographs). The horizontal convection velocity is the same for both halves. One is therefore following the eddies on the upper and lower halves. (Cantwell, Coles & Dimotakis 1978) plotted the data taken at three stations for a turbulent spot using conical similarity coordinates, with the view of collapsing the results. In the cases examined here, the growth is only in the vertical direction. Some of the structures are also changing their topology and similarity would not really be applicable). The discontinuity in vertical convection velocity is not evident at all in the vector fields. This is probably due to the vertical convection velocity being small compared with the velocity magnitudes along the streamwise axis of the jet.

From an examination of the vector fields and the mean-velocity profiles, bifurcation appears to be occurring not only in the jet shown in figure 9, but also at the downstream end of the jet shown in figure 8. In both cases, bifurcation is accompanied by the formation of mushroom-like structures from single-loop types. These are sketched in figure 10. The mushroom-like structures are actually vortex rings seen in cross-section. One of the surprising features of the patterns shown in figure 8 (*c*) is the presence of foci with flow spiralling out. This implies that vortex filaments are being compressed, which is contrary to what one would expect in developing flow. Perry *et al.* assumed vortex stretching in their interpretations, giving foci with the flow spiralling in. This appears to be correct for single-sided structures but not for double-sided structures. It appears in general that double-sided structures with single loops consist mainly of foci where the flow spirals out. The flow in some of the foci in both jets also appear to spiral out to limit cycles, i.e. singular closed streamlines.

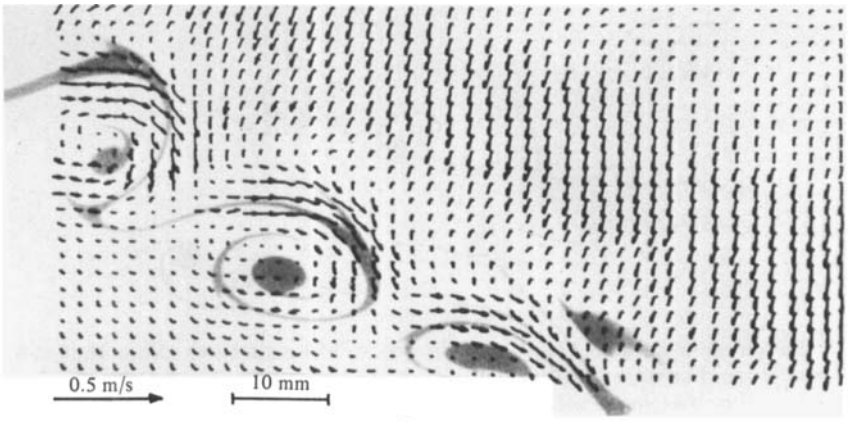

(a)

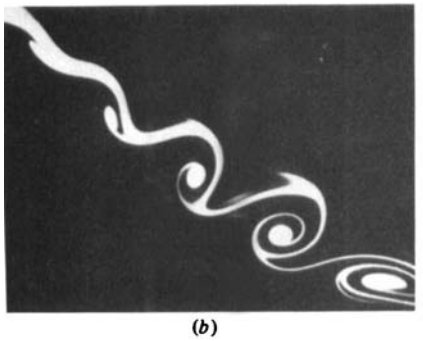

(b)

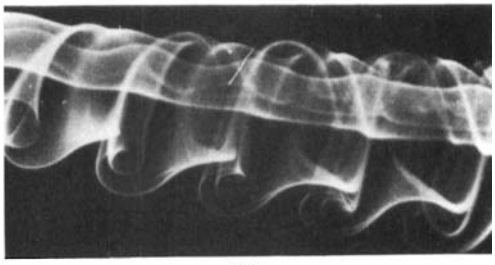

(c)

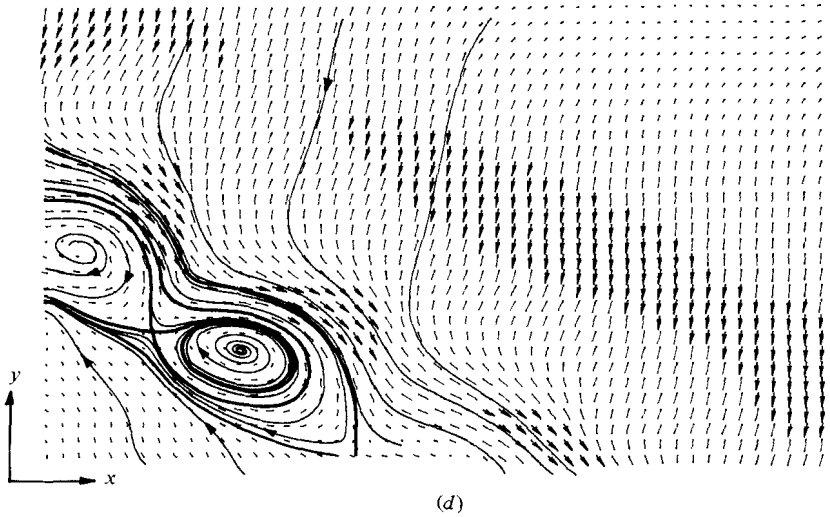

(d)

FIGURE 11. Single-sided (negatively buoyant) jet. (*a*) Vector field superimposed on smoke photograph (smoke photograph is shown in negative for clarity). (*b*) Laser-sectioned photograph. (*c*) Externally illuminated photograph. (*d*) Streamline pattern computed from vector field shown in (*a*). Vector field shown is that obtained from the tiling procedure. $U_\infty \approx 0.11$ m/s, $U_\psi \approx 0.124$ m/s, $V_\psi \approx -0.081$ m/s, $f \approx 6.9$ Hz.

In figure 9(*b*) it is seen that interconnecting pairs of foci, with flow spiralling in and out, occur after bifurcation has commenced.

Figures 11(*a–d*) show a single-sided (negatively buoyant) jet. The properties of this structure were anticipated by Perry & Lim in their classification, but they had failed to produce it with sufficient steadiness. It was very difficult to generate and obtaining the vector field was really a test of the experimental technique (the freestream velocity was only 0.11 m/s). The streamline pattern is very much like that conjectured by Perry *et al.* The second vortex shown in figure 11(*d*) appears to have flow spiralling in 'in the large', but, at the focus, trajectories spiral out to a limit cycle. This feature differs from what was anticipated by Perry *et al.*

3.2. *Vorticity distribution*

Vorticity distributions were obtained by computing the mean of the differences in velocity between points in the centre of a rectangular cell. Each cell was comprised of 9 points, including the point at the centre. Cell sizes were typically 1×2 mm. Since the data had been smoothed, the vorticity distributions computed by this method had tolerable scatter.

Plots of the vorticity distribution were done on a Tektronix 5113 dual-beam storage scope. The intensity of the scope was used to represent the magnitude of the vorticity at each point. Brighter points represent higher absolute values of vorticity.

Figure 12 shows the vorticity distribution of the structures measured. The concentrations of vorticity correspond to the foci in the flow. The formation of mushroom-like structures can clearly be seen, as the vorticity concentrations break up into positive/negative pairs. If a succession of clumps of smoke along either the top or bottom half of the jets shown in figures 12(*b*) or (*c*) are inspected, it will be noted that, at the upstream end, each clump of smoke corresponds to a patch of vorticity of one sign. Further downstream, however, each clump of smoke corresponds to a pair of positive and negative areas of vorticity.

3.3. *Vortex pairing*

The interest in vortex pairing arose with investigations into organized structures in turbulent shear flow. Studies have been made of pairing in shear layers and in axisymmetric jets. The work shows that it plays an important role in the behaviour of the flows studied (e.g. in their growth, entrainment, production of Reynolds stress, noise production, etc.; see e.g. Brownand & Weidman 1976; Brown & Roshko 1974, Zaman & Hussain 1980; Acton 1976, 1980). The investigations so far have been limited to basically two-dimensional flows. Since a great number of flows of interest and practical importance are three-dimensional, the question naturally arises as to whether vortex pairing plays a role in their development and behaviour, or, indeed, whether it occurs at all. Since the negatively buoyant wake structures were the simplest patterns to produce with high periodicity, it was decided to attempt to induce them to pair.

The technique of Ho & Huang (1982) was used. They had induced pairing and 'collective interaction' (i.e. coalescing of any number of eddies) of two-dimensional structures in a plane mixing layer by exciting the flow at a fundamental frequency and various subharmonics. A negatively buoyant wake was stimulated at two frequencies (f and $2f$) with the circuit shown in figure 3. Figures 13(*a–c*) show externally illuminated and laser-sectioned photographs of the structures produced. The flow appears to consist of a series of alternating large and small eddies, which appear to be pairing or merging.

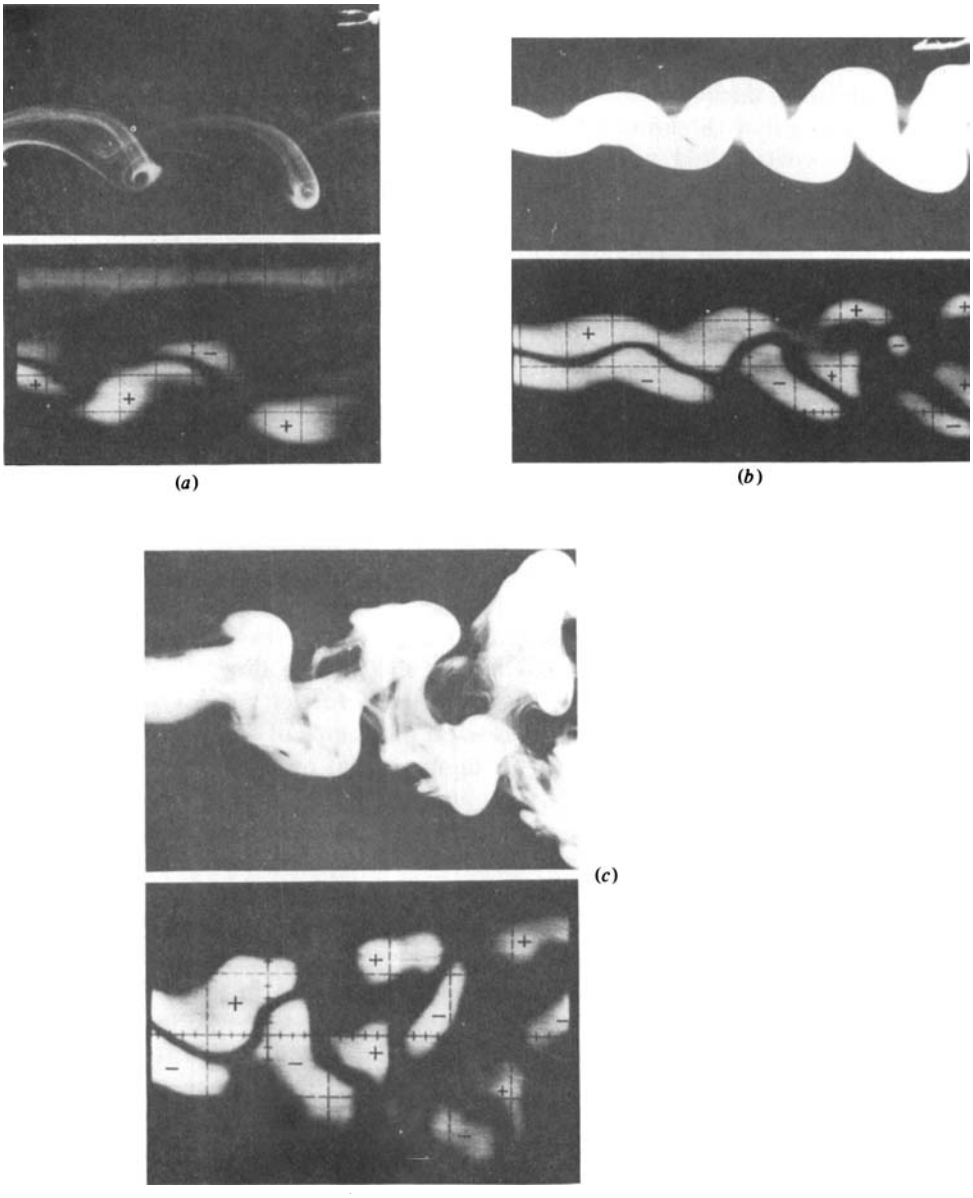

FIGURE 12. Smoke photographs together with their respective vorticity distributions for: (*a*) negatively buoyant wake; (*b*) double-sided jet; (*c*) double-sided jet (bifurcating). Smoke photographs and vorticity distributions are printed to the same scale. + and − signs on the vorticity plots indicate regions of positive and negative vorticity.

The data sampling and processing was based on the lower frequency of tube oscillation. Two distinct peaks occurred in the correlation coefficient R, as seen in figure 14. These peaks correspond to the convection velocities of the larger and smaller eddies, the larger peak corresponding to the larger eddies. The larger eddies are, in effect, overtaking the smaller eddies. This can be clearly seen in the smoke photographs and in figures 15(*a–c*), which show the pairing event in a sequence of vector fields of different phases. The computed streamline pattern is shown together

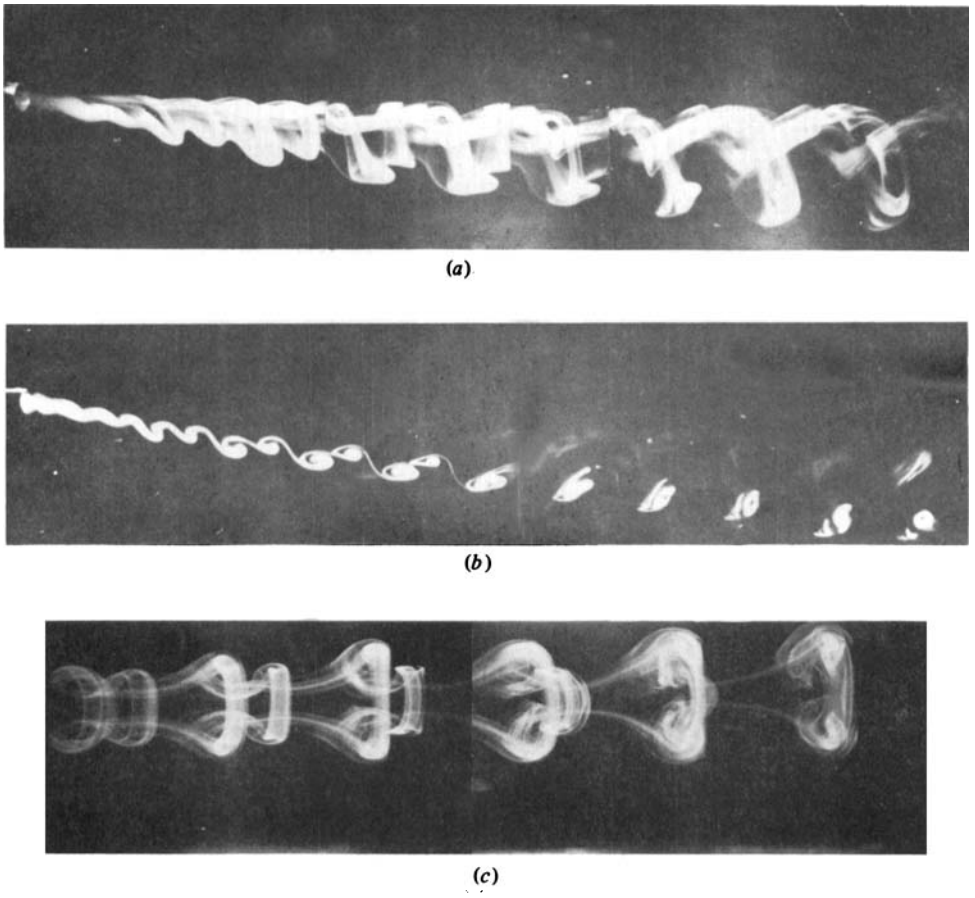

FIGURE 13. Vortex pairing: (*a*) externally illuminated photograph; (*b*) laser-sectioned photograph; (*c*) externally illuminated plan view (i.e. in $-y$-direction).

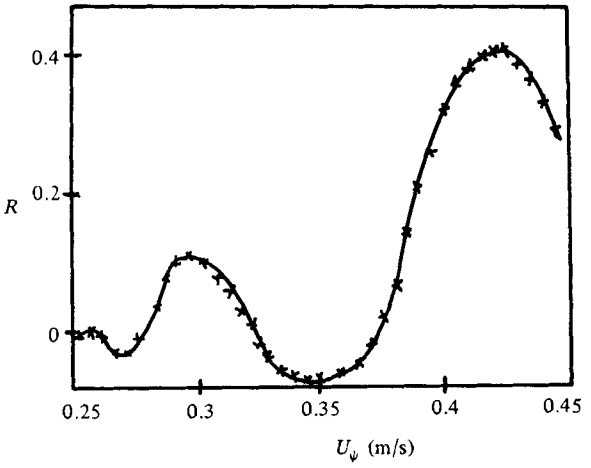

FIGURE 14. Horizontal convection velocity U_ψ versus correlation coefficient R for a typical level.

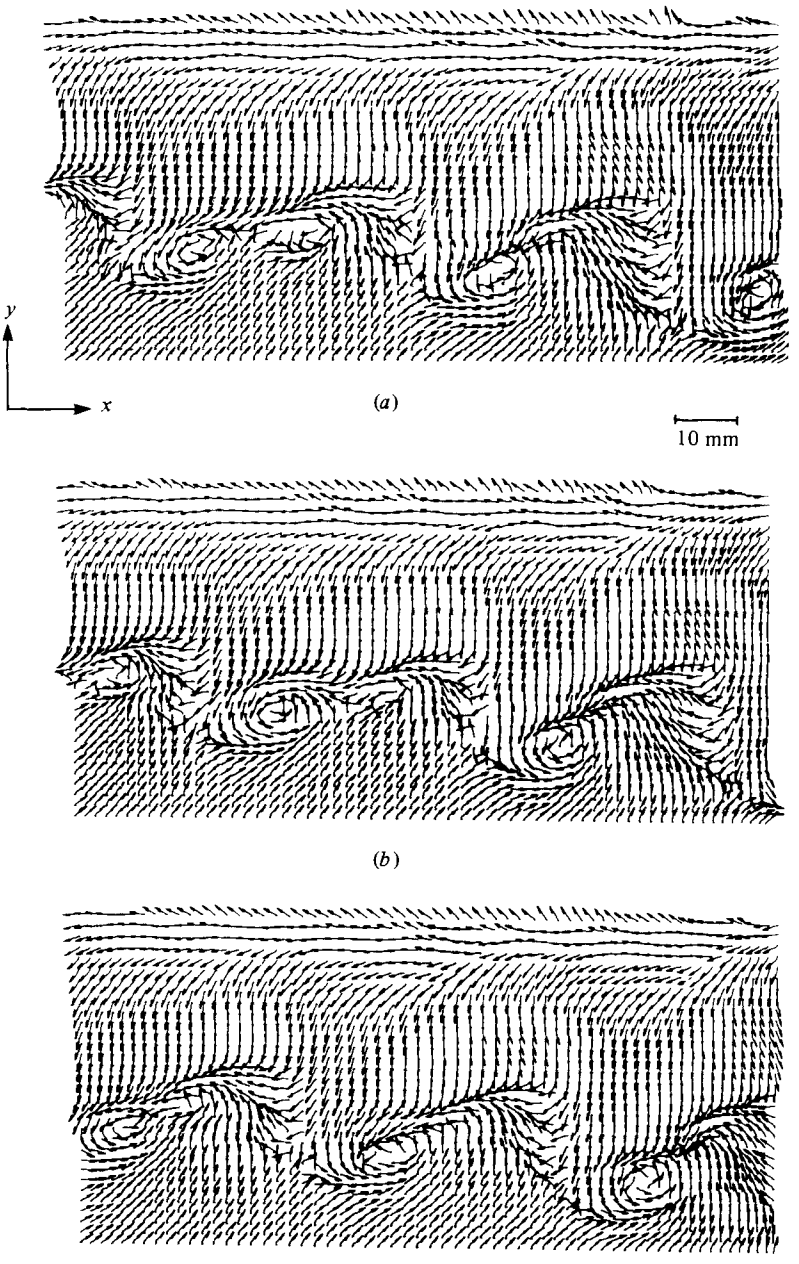

FIGURE 15. Vector fields showing the pairing process (only the directions of the vectors are shown): (*a*) phase 1; (*b*) phase 10; (*c*) phase 20. $U_\infty \approx 0.36$ m/s, $U_\psi \approx 0.33$ m/s, $V_\psi \approx -0.09$ m/s, $f \approx 7$, 14 Hz, Reynolds number (based on U_∞) ≈ 320.

with the vorticity distribution in figures 16(*a*, *b*). The smaller downstream eddy of each 'pair' begins to rotate around the larger upstream eddy and then appears to merge into it. The vorticity distribution shows this as well, with the vorticity concentrated at the foci in the flow. Only the positive values of vorticity have been shown. An interesting point to note is that the pattern above the structures corresponds with that of figure 7 rather than that of figure 6(*c*).

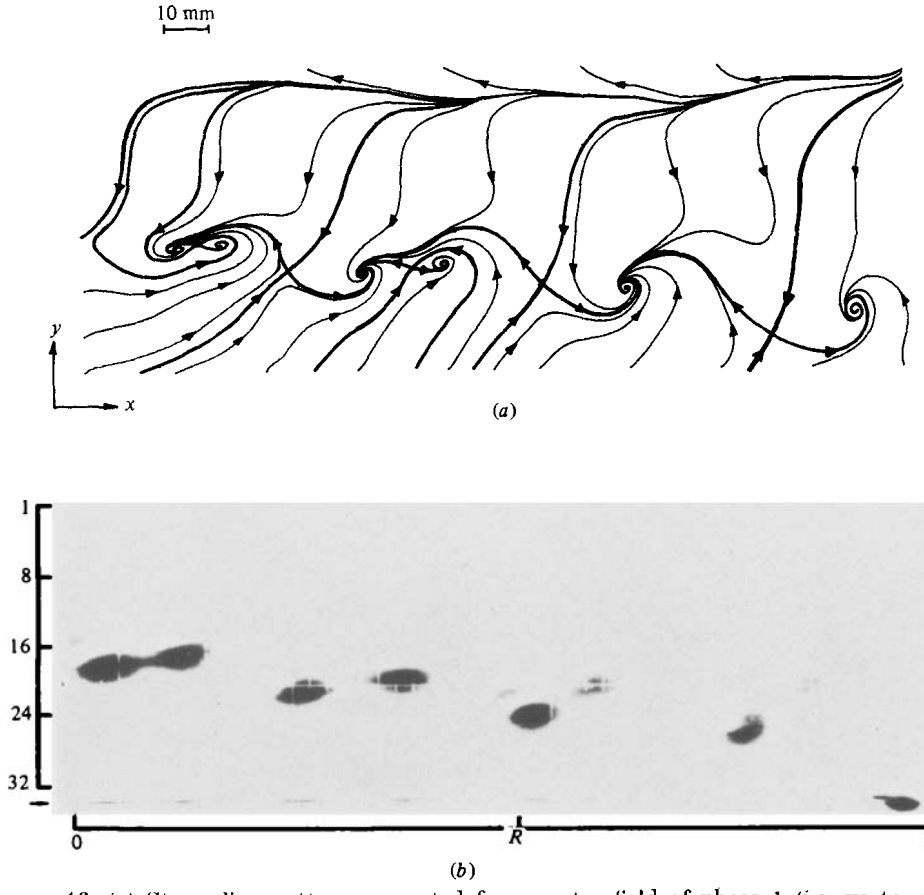

FIGURE 16. (*a*) Streamline pattern computed from vector field of phase 1 (i.e. vector field in figure 15*a*); (*b*) Vorticity distribution of phase 1. R is the crank radius. Numbers on the vertical axis indicate different y-levels.

Unfortunately, the working section of the tunnel used was too short for an attempt at inducing collective interaction. Further work on this may be pursued in the future.

3.4. *Spectrum of an eddy*

Recently, Perry & Chong (1982) have proposed a model for the mechanism of wall turbulence which gives a connection between the mean velocity distribution, the broad-band turbulence intensity distribution and the turbulence spectra. They found that the salient features of the spectrum (i.e. the power spectral density (p.s.d.)) could be generated from the velocity signatures existing in the irrotational fluid surrounding the vortex rods of simple 'horseshoe', 'hairpin' or 'lambda' vortices. In the simple case of a straight vortex filament of infinite length of arbitrary orientation, they predicted that the u-signature (i.e. streamwise component) would have an even 'bell'-shaped function and the v-signature (i.e. vertical component) would have a shape that is a combination of an even and an odd function. The p.s.d. of a periodic array of such u- and v-signatures would be a series of peaks spaced at frequencies in arithmetic progression. It can be shown that the peaks have an exponential envelope. A 'smoothed' p.s.d. for a random array of such signatures would be proportional to this exponential envelope.

The negatively buoyant wake was an easily generated eddy which was fairly large (relative to a hot wire). Close to the eddy, the smoke 'scroll', corresponding to a

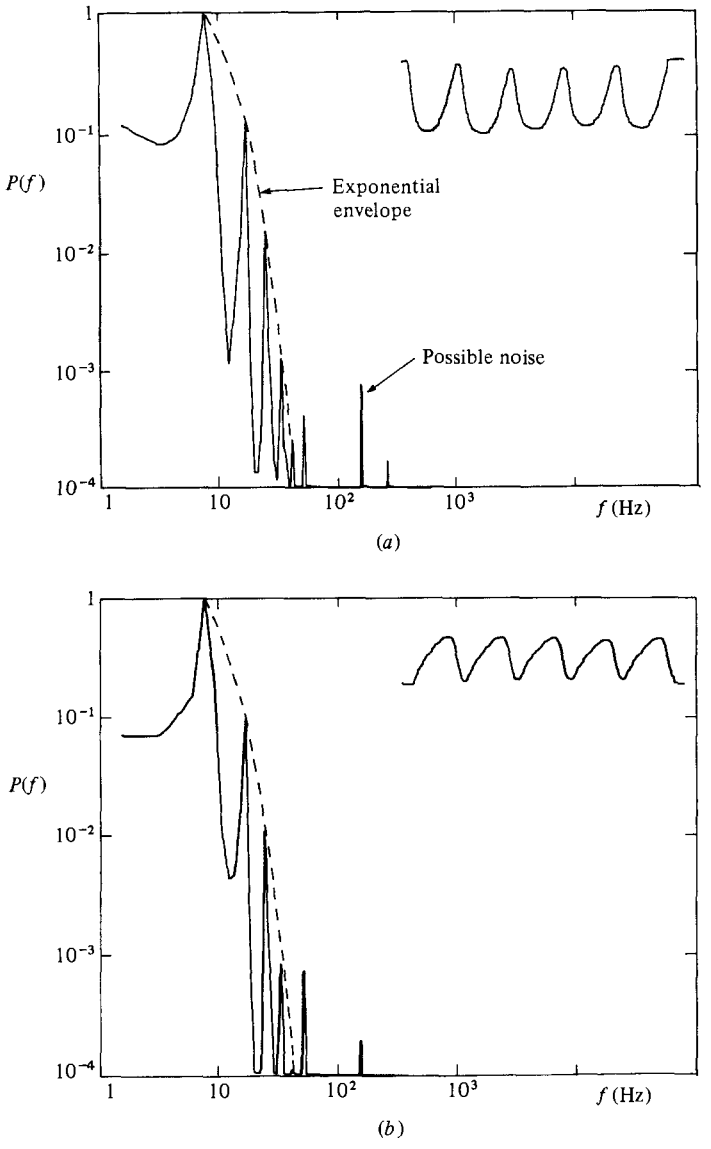

FIGURE 17 (*a*, *b*). For caption see facing page.

focus in figure 6, could therefore be likened to a straight vortex rod of infinite length (orientated normal to the plane of the page). With this particular orientation of the vortex filament, the u-signature should be an even bell-shaped function and the v-signature should be an odd function. The velocity signatures and spectra were taken close to and inside the rods of a train of negatively buoyant wake-type eddies. The results are shown in figures 17 (*a–d*). The signals outside the scroll do follow bell and odd-function shapes. The corresponding p.s.d.s have exponential envelopes with the peaks going in an arithmetic progression. These were obtained with a standard fast-Fourier-transform program. Once inside the rod, the p.s.d.s depart from exponential envelopes. The signatures are still of the same basic shapes, with distortions introduced by the vorticity.

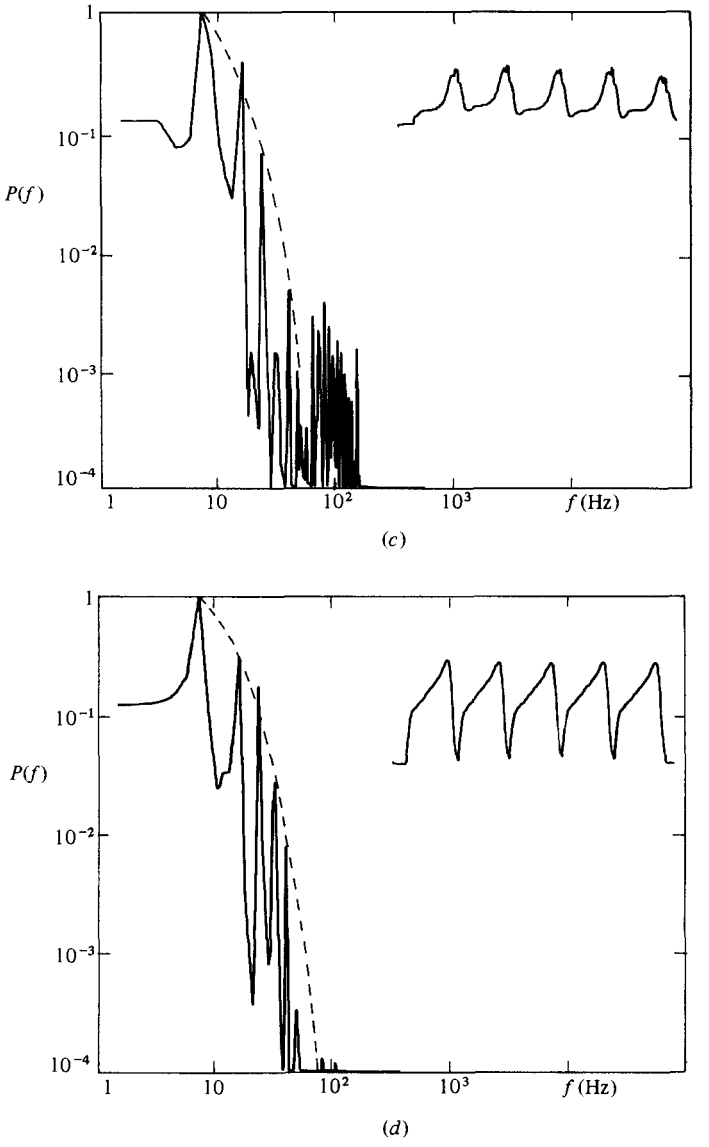

FIGURE 17. Velocity signatures and p.s.d.s for (*a*) *u*-signal, (*b*) *v*-signal just below the scroll and (*c*) *u*-signal. (*d*) *v*-signal through the scroll. All p.s.d.s have their maximum normalized to 1. Exponential envelopes are of form $\ln P(f) = A - 2\,\mathrm{e}^{\ln f}$.

An interesting feature of the *u*-signature is the top of the bell. If solid-body rotation is assumed within the rod, a bell shape with a flat top would be expected. Instead, the top appears to be jagged. This is possible, since the jagged effect could be caused by the individual vortex sheets in the rod. Figure 18 shows how a series of concentric shells of vorticity (assuming this to represent a scroll) can produce a jagged top. Such a velocity signature is computed using the Biot–Savart law.

To verify that the jagged top was indeed caused by the sheets and not by some other factor(s) due to the crossed wires, the signal through a scroll was taken by a single normal wire which was aligned parallel to the vorticity vector. The spectrum at high frequencies is influenced mainly by the fine-scale features of the eddy

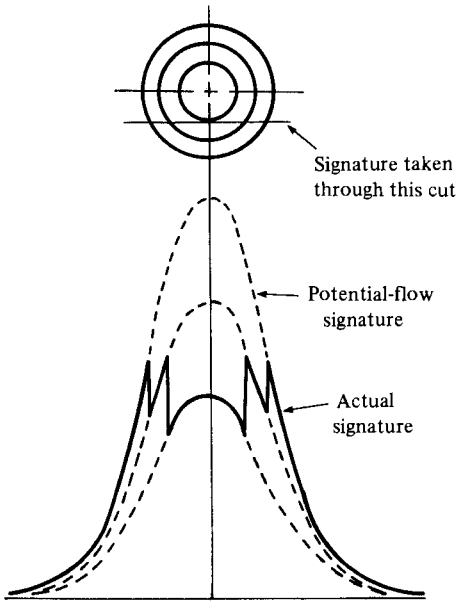

FIGURE 18. Sketch showing sawtooth-top u-signature, produced from a scrolled rod.

signature. According to Bracewell (1978), if n is the number of times a signal has to be differentiated to convert it to a delta function, the smoothed p.s.d. $P(k)$ will asymptote to a law $P(k) \sim k^{-2n}$, where k is the wavenumber or frequency. The p.s.d. through a scrolled rod should have a -2 slope, since a sawtooth function has to be differentiated once to obtain a delta function. Figures 19(a, b) show the p.s.d. taken with a normal wire and a closeup of the jagged top. It does appear to have a -2 slope. As a further check, the high-frequency ends of the other signals without the jagged top were examined. No -2 slopes were present. Figure 20 shows the signature and spectra taken through a scroll three wavelengths further downstream. There is no jagged top, implying that the vortex sheets in the scroll have completely smeared out. The spectral peaks appear to follow an exponential envelope more closely.

3.5. *Modelling of structures with vortex skeletons*

Although the vector fields for the wake and jets examined so far reveal the features of the flow fairly clearly, there was still the problem of selecting the appropriate convection velocity for viewing the patterns. A better method of describing the flows would be one that utilized a quantity that was invariant with the velocity of the observer. This can be done by looking at the vorticity distribution of the flow.

For the flows examined here, the authors content that the vorticity can be assumed to be confined to rods of small diameter, and a vortex skeleton can be constructed using the measured vorticity and smoke photographs as a guide. Once the skeleton has been selected, the velocity field can be computed using the Biot–Savart law and comparisons made with the measured velocity fields. The skeleton can be fairly crude. Curved loops can be replaced with straight segments. The junction between segments are singularities but these have small far-field effects, and hence the topological features of the velocity field away from such corners should be approximately correct. The rods were assumed to have circular cross-sections of finite diameter (diameters are given in the figures), but for the purposes of calculating the flowfield outside the

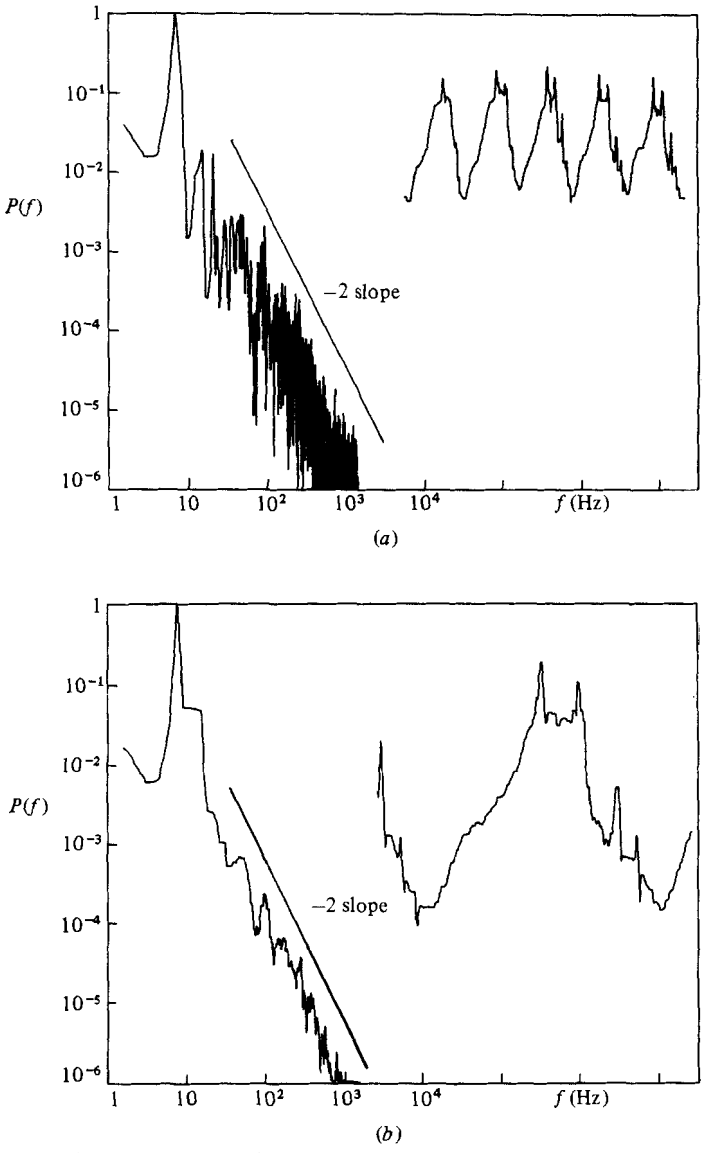

FIGURE 19. (*a*) *u*-signature and p.s.d. taken with a normal wire. (*b*) Same results as (*a*) except p.s.d. has been smoothed (signature shown is an enlargement of the third peak shown in *a*).

rods with the Biot–Savart law, the rods were assumed to have zero diameter. The flows inside the rods were computed by assuming that all velocity components varied linearly between the two ends of any chord which crossed the rod boundaries.

The vortex-skeleton configuration used for the negatively buoyant wake is shown in figure 21. It is made up of a collection of straight-sided closed loops, each having the same circulation. Closed loops were used to satisfy the solenoidal condition for vorticity. Rod 1 consists of a bundle of filaments which are assumed to be smeared into a circular rod of 0.12 units radius. On the side 'arms' the filaments can be assumed to be coincident. Rods 2–8 were distributed as shown in the figure and actually simulate a vortex sheet. Rod 1 will therefore have a circulation seven times

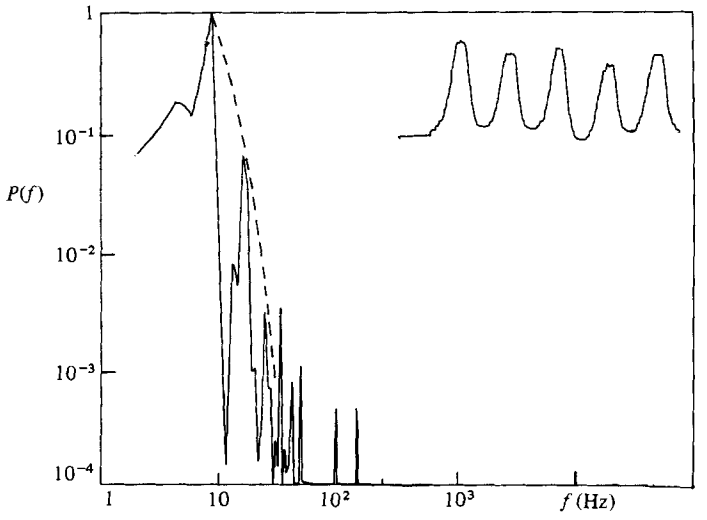

FIGURE 20. u-signature and p.s.d. taken three wavelengths further downstream.

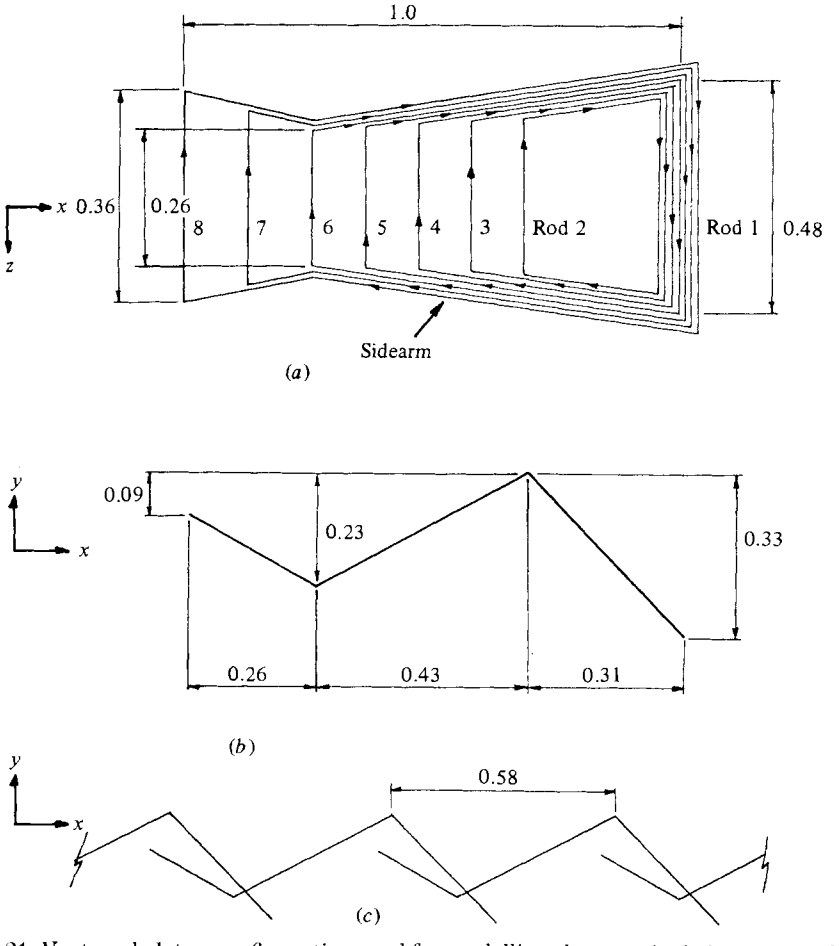

FIGURE 21. Vortex-skeleton configuration used for modelling the negatively buoyant wake: (*a*) plan view; (*b*) elevation; (*c*) location of structures (radius of rod 1 assumed to be 0.12 units, radii of rods 2–8 assumed to be 0.05 units).

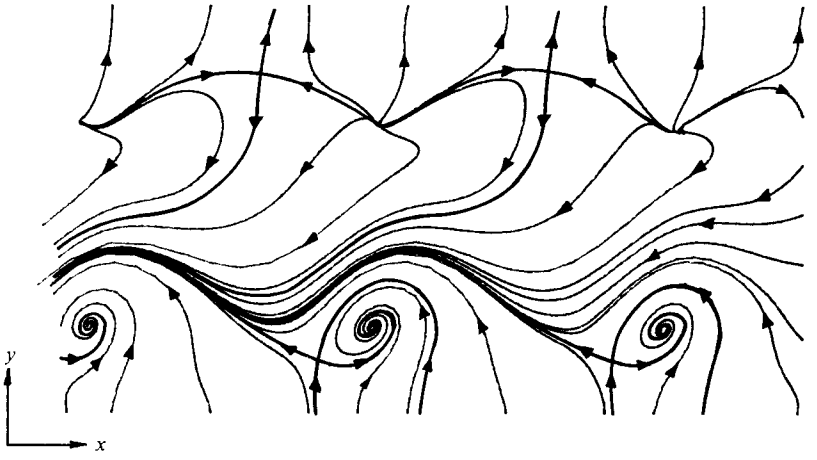

FIGURE 22. Streamline pattern computed from the vector field produced by the model for the negatively buoyant wake.

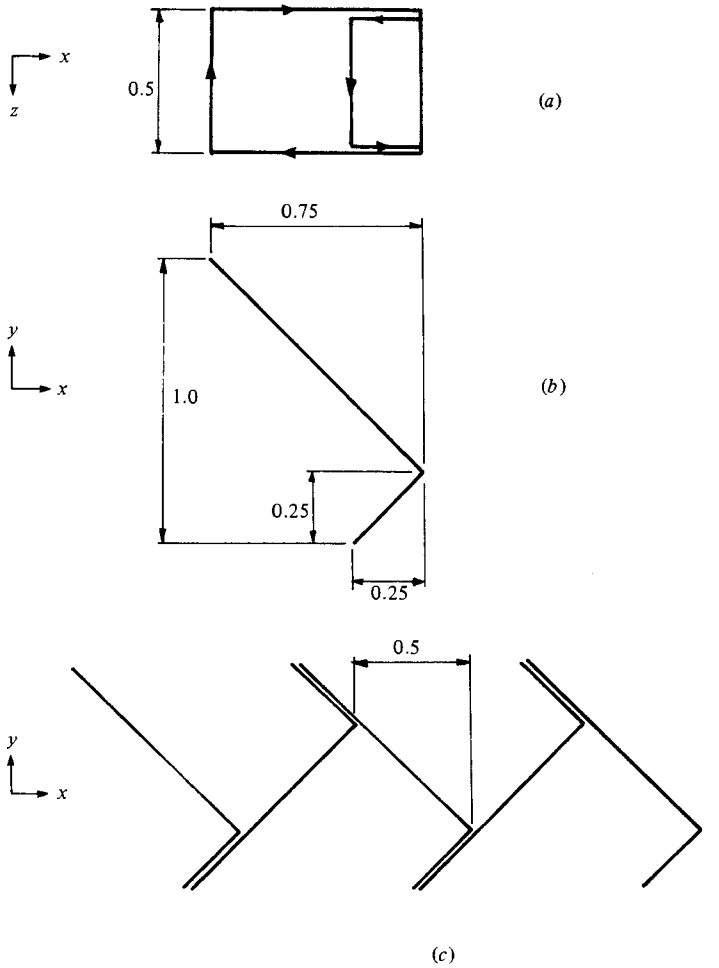

FIGURE 23. Vortex-skeleton configuration used for modelling the double-sided jet: (*a*) plan view; (*b*) elevation; (*c*) location of structures (radii of all rods were assumed to be 0.1 units).

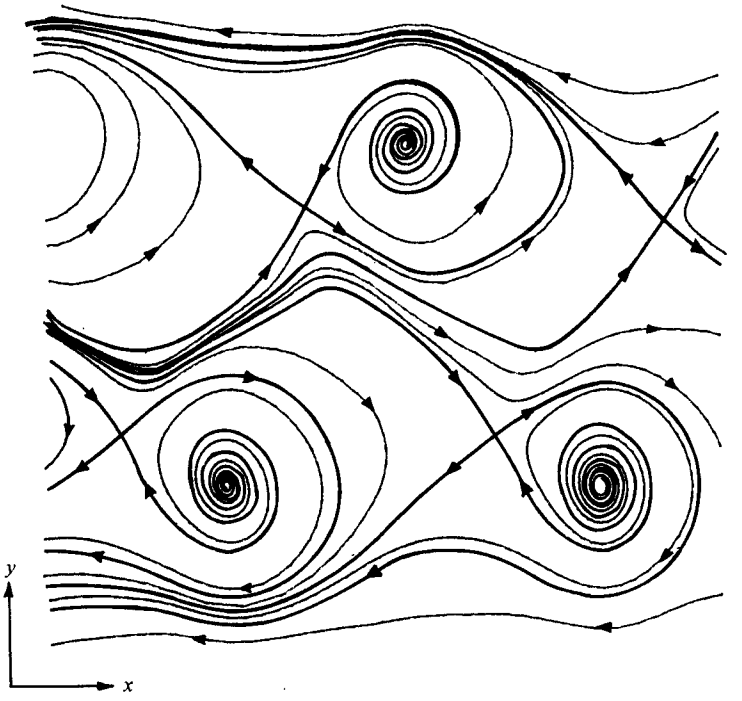

FIGURE 24. Streamline pattern computed from the vector field produced by the model for the double-sided jet.

that of rods 2–8. The sidearms are, in effect, rods whose circulations increase as they approach rod 1.

The velocity distribution on the plane of symmetry about the third structure, in a train of five structures, was computed. There was some difficulty with the selection of an appropriate convection velocity because different parts of the structure had different induced velocities.

Figure 22 shows the computed streamline pattern as seen by an observer moving with a velocity close to the induced velocity of rod 2. This pattern is similar to the experimental result given in figure 6(*c*), but the foci and saddles are distorted. This is probably due to an incorrect choice of vorticity distribution. Such a distribution should include the streamwise growth of the structures and be such that the horizontal convection velocity of all parts of the structures are approximately the same, as was found in the experimental results. The number of alternative modifications was too great to attempt here and the result shown in figure 22, although not perfect, is encouraging. Mean velocities and Reynolds stress profiles calculated from the model were compared with experimental results and again the agreement was also encouraging (see Tan 1983).

The vortex configuration used for the neutrally buoyant jet is shown in figure 23. This serves to simulate the jet before bifurcation and the resulting streamline pattern about the fifth structure in a train of nine was computed and is shown in figure 24. The streamwise growth has not been included. The horizontal convection velocity of the cross-stream vortices was used. A vertical convection velocity was not used since it is important only when the jet is bifurcating. It can be seen that the model results bear a strong resemblance to the experimental results and the flow spirals out

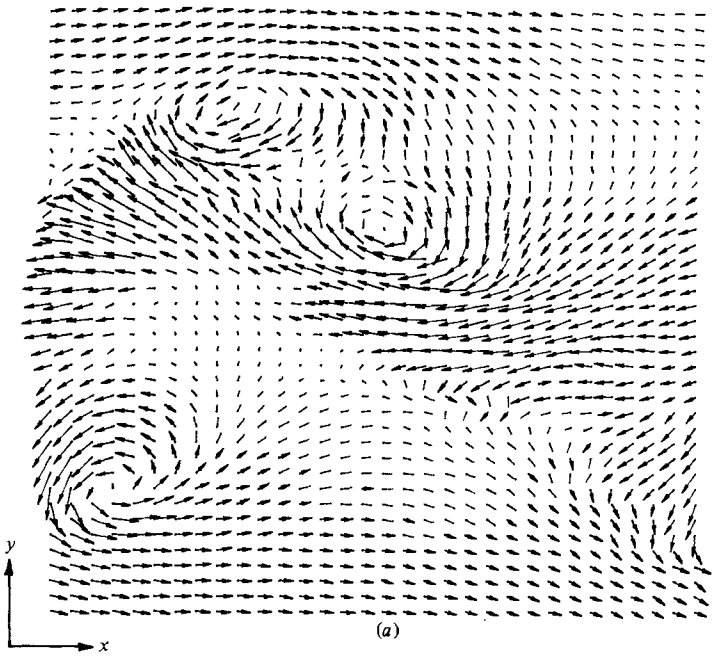

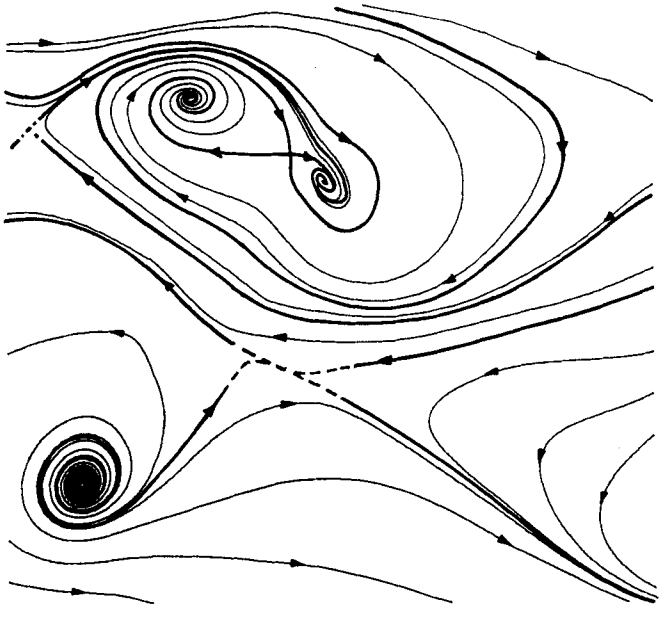

FIGURE 25. (*a*) Experimental results of Perry *et al.* for a neutrally buoyant wake. (*b*) Streamline pattern computed from vector field shown in (*a*).

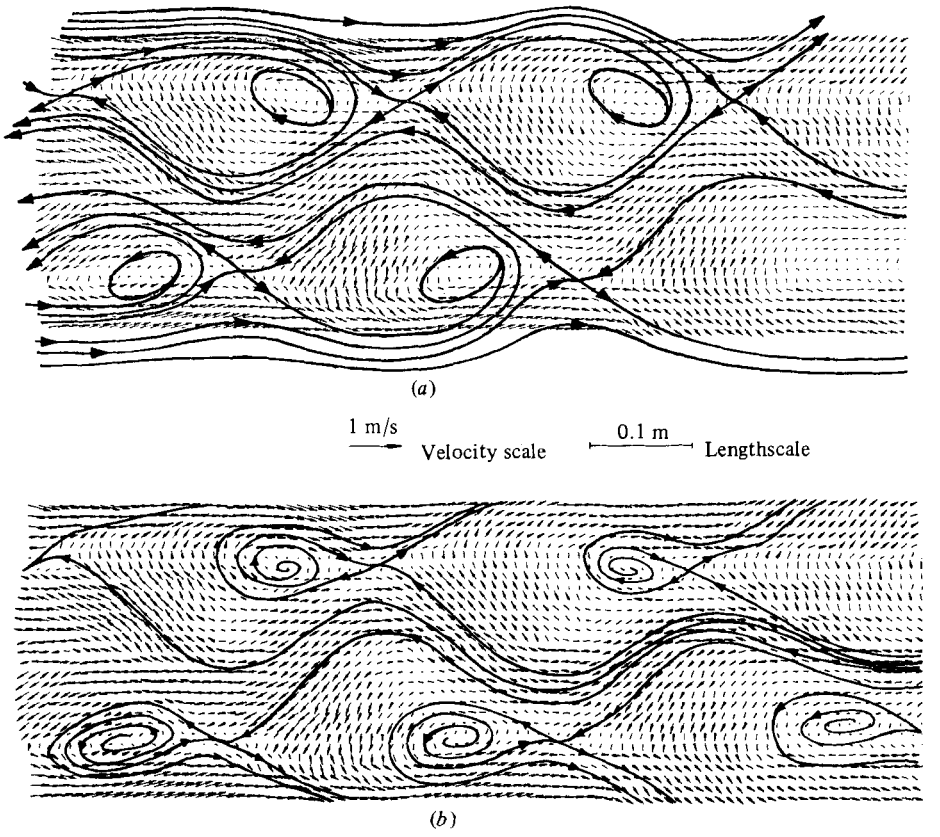

FIGURE 26. Experimental results obtained by Perry & Watmuff for the wake behind an ellipsoidal body: (*a*) Perry & Watmuff's interpretation of the streamline pattern; (*b*) authors' interpretation of the streamline pattern.

of the foci. By rotating the pattern shown in figure 24 by 180° about the y- or z-axes, the flowfield for a double-sided wake is obtained. Note, however, that the flow spirals out of the foci, which is at variance with the interpretations of Perry *et al.* (1980) and Perry & Watmuff (1981).

Figure 25(*a*) shows the experimental results for a neutrally buoyant wake obtained by Perry *et al.* Unfortunately they were unable to remove the double eddy that occurs on the upper half of the flowfield. The streamline pattern for these results were computed using the technique described earlier and the result is shown in figure 25(*b*). Flow spirals into the foci on the upper half of the flowfield, but on the lower half the flow spirals out of the foci. There is an obvious lack of symmetry in this flow. The authors had attempted to produce a neutrally buoyant wake but had failed in producing one with sufficient steadiness. Note that large amplitudes of tube oscillation are required to produce such flows (typically $v'/U_\infty \approx 0.5$). Alternatively, such patterns can be produced behind vortex-shedding bodies. Note the 'strong' dislocated saddle. (This has been shown with dashed lines since it was drawn in by eye. The program had failed to compute the streamlines close to the saddle owing to the extremely small numbers involved.) A better-behaved neutrally buoyant wake (i.e. without the double eddy) was obtained by Perry & Watmuff. This was a fully turbulent, high-Reynolds-number (33000) flow behind an ellipsoidal body. The

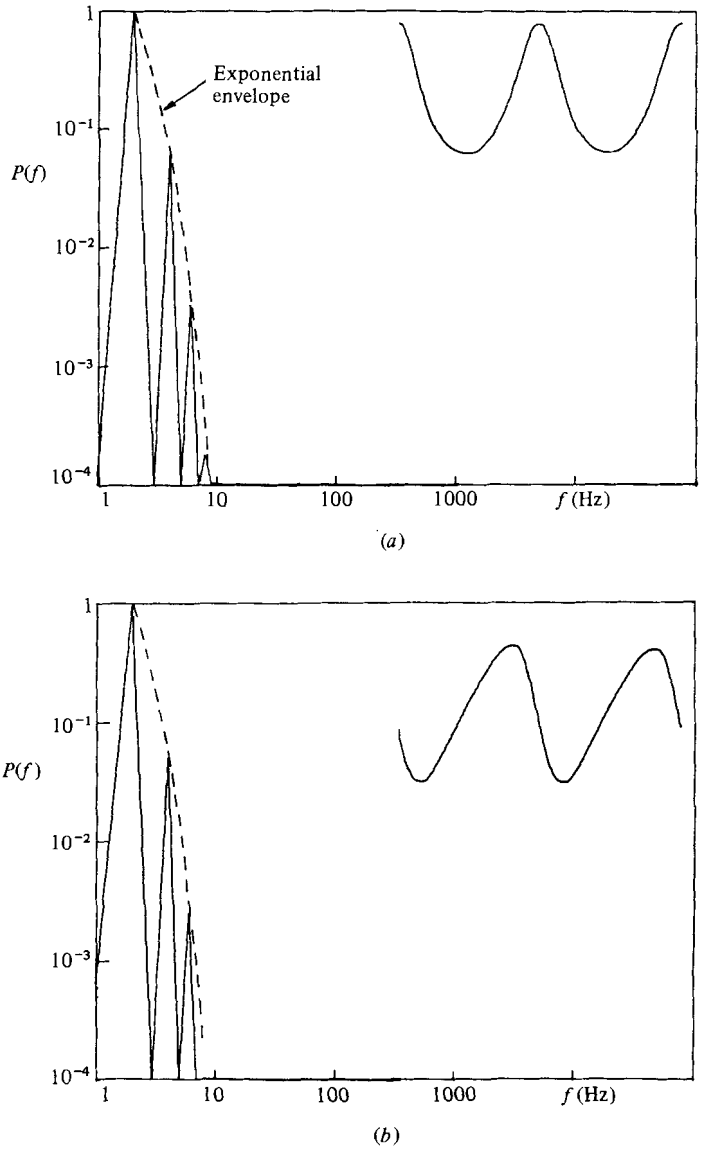

FIGURE 27. Velocity signatures and spectra of model for the negatively buoyant wake at a position 0.13 units below the position of rod 1: (*a*) *u*-signature and spectrum; (*b*) *v*-signature and spectrum.

vector field was obtained from data sampled and averaged on the basis of the phase of the vortex shedding from the body. Figure 26(*a*) shows the vector field obtained by Perry & Watmuff, together with their interpretation of the streamline pattern. The streamline pattern was sketched in with the preconceived idea that the flow had to spiral into the foci. Figure 26(*b*) shows an alternative interpretation with flow spiralling out of the foci, as suggested by the vortex-skeleton model. It can be seen that this interpretation fits the data much better.

The velocity signatures and spectra of the vortex-skeleton model for the negatively buoyant wake were also computed. These are shown in figure 27 and agree well with the experimental results.

4. Conclusion

The experimental technique described allowed entire velocity vector fields in a plane through perfectly periodic eddying motions to be measured and related to the smoke pictures produced from flow visualization. The technique did not rely on any assumptions concerning Taylor's hypothesis, and so allowed rapidly developing patterns to be examined in detail. It was also used to study three-dimensional vortices, which were induced to pair using the technique of Ho & Huang (1982).

Instantaneous streamline patterns were obtained by integrating the vector field of one phase, and the topology of the patterns were conveniently described in terms of critical points. Many of the interpretations of Perry *et al.* (1980) and Perry & Watmuff (1981) require modification. In particular, the patterns observed are very sensitive to the convection velocity of the observer. By a careful determination of this convection velocity, the pattern for negatively buoyant wakes was found to be different from that given by Perry *et al.* It was also found that single-sided structures have foci where the flow spirals in, whereas double-sided structures appear to have foci where the flow spirals out. (There are some exceptions to this, which the authors cannot explain at the moment.) Thus in developing flow, vortex stretching is not the only process involved – vortex compression is also possible.

Coflowing jets that bifurcated exhibited very complex patterns where simple vortex loops develop into mushroom-like structures. In these instances, both types of foci were found to occur with limit cycles.

The velocity signatures and power-spectral densities of a train of negatively buoyant wake eddies was obtained. The results show that, close to the foci, the u-signatures of the eddies are an even bell-shape function whilst the v-signatures are odd functions. Their corresponding p.s.d.s consist of series of peaks going in arithmetic progression with exponential envelopes. The results agreed with the theoretical results obtained from potential flow vortices. Vortex sheets within the eddies gave rise to the expected -2 power law p.s.d.

The simplest patterns observed have been described with vortex skeleton models. Using the Biot–Savart law, the velocity vector fields and instantaneous streamline patterns were reproduced with encouraging success. In fact, such models correctly predicted the behaviour of the foci. They also gave the correct spectral behaviour for the velocity signatures which they generated.

The authors wish to acknowledge the financial assistance of the Australian Research Grants Scheme, the National Energy Research, Development & Demonstration Program and the Australian Institute of Nuclear Science & Engineering. The authors also wish to acknowledge the assistance of Drs M. S. Chong and T. T. Lim during the course of this work.

REFERENCES

Acton, E. 1976 The modelling of large eddies in a two-dimensional shear layer. *J. Fluid Mech.* **76**, 561.

Acton, E. 1980 A modelling of large eddies in an axisymmetric jet. *J. Fluid Mech.* **98**, 1.

Anderson, J. M. 1981 The structure and dynamics of periodically stimulated jets and wakes. M.Eng.Sc. thesis, University of Melbourne.

Batchelor, G. K. 1967 *An Introduction to Fluid Dynamics.* Cambridge University Press.

Bracewell, R. N. 1978 *The Fourier Transform and its Application*, 2nd ed. McGraw-Hill.

BROWAND, F. K. & WEIDMAN, P. D. 1976 Large scales in the developing mixing layer. *J. Fluid Mech.* **76**, 127.

BROWN, G. L. & ROSHKO, A. 1974 On density effects and large structure in turbulent mixing layers. *J. Fluid Mech.* **64**, 775.

CANTWELL, B. J., COLES, D. & DIMOTAKIS, P. 1978 Structure and entrainment in the plane of symmetry of a turbulent spot. *J. Fluid Mech.* **87**, 641.

DAVIES, P. A. O. L. & YULE, A. J. 1975 Coherent structures in turbulence. *J. Fluid Mech.* **69**, 513.

FALCO, R. E. 1977 *Phys. Fluids Suppl.* **20**, S124.

HO, C. M. & HUANG, L. S. 1982 Subharmonics and vortex merging in mixing layers. *J. Fluid Mech.* **119**, 443.

HORNUNG, H. & PERRY, A. E. 1982 Streamsurface bifurcation, vortex skeletons and separation. *DFVLR Internal Rep.* IB 222–82 A25.

KLINE, S. J. 1965 *Film Loop FM-48*. National Committee for Fluid Mechanics Films.

PAO, H. P. & KAO, T. W. 1977 Vortex structure in the wake of a sphere. *Phys. Fluids* **20**, 187.

PERRY, A. E. 1982 *Hot-Wire Anemometry*. Clarendon.

PERRY, A. E. & CHONG, M. S. 1982 On the mechanism of wall turbulence. *J. Fluid Mech.* **119**, 173.

PERRY, A. E. & FAIRLIE, B. D. 1974 Critical points in flow patterns. *Adv. Geophys.* **B18**, 299.

PERRY, A. E. & LIM, T. T. 1978*a* Coherent structures in coflowing jets and wakes. *J. Fluid Mech.* **88**, 451.

PERRY, A. E. & LIM, T. T. 1978*b* *Eddies in Captivity* (16 mm colour/sound film). Centre for the study of Higher Education, University of Melbourne.

PERRY, A. E., LIM, T. T. & CHONG, M. S. 1980 The instantaneous velocity fields of coherent structures in coflowing jets and wakes. *J. Fluid Mech.* **101**, 243.

PERRY, A. E. & WATMUFF, J. H. 1981 The phase-averaged large-scale structures in three-dimensional turbulent wakes. *J. Fluid Mech.* **103**, 33.

ROSHKO, A. 1954 On the development of turbulent wakes from vortex streets. *NACA Rep.* 1191.

TAN, D. K. M. 1983 Simple three-dimensional vortex motions in jets, wakes and boundary layers. Ph.D. thesis, University of Melbourne.

TOWNSEND, A. A. 1951*a* On the fine-scale structure of turbulence. *Proc. R. Soc. Lond.* A **208**, 534.

TOWNSEND, A. A. 1951*b* The diffusion of heat spots in isotropic turbulence. *Proc. R. Soc. Lond.* A **209**, 418.

ZAMAN, K. B. M. Q. & HUSSAIN, A. K. M. F. 1980 Vortex pairing in a circular jet under controlled excitation. Part 1. General jet response. *J. Fluid Mech.* **101**, 449.